Inorganic Chemistry Communications 175 (2025) 114012

Contents lists available at ScienceDirect

Inorganic Chemistry Communications

journal homepage: www.elsevier.com/locate/inoche

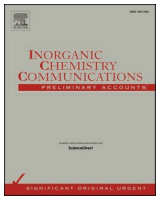

Box-Behnken Design Optimization of photocatalytic performance of $ZnWO_4$ nanoparticles multiple doped with selected metals

Hassana Ladio Abubakar [a,c], Jimoh Oladejo Tijani [a,d,*], Saheed Mustapha [a,d], Ambali Saka Abdulkareem [b,d], Mann Abdullahi [a], Titus Chinedu Egbosiuba [e], Francis Ntumba Muya [f], Omar H. Abd-Elkader [g], Hamad A. Al-Lohedan [h], Alechine Emmanuel Ameh [f,i], Abdelrahman O. Ezzat [h,**]

[a] Department of Chemistry, Federal University of Technology, PMB 65, Minna, Niger State, Nigeria
[b] Department of Chemical Engineering, Federal University of Technology, PMB. 65, Minna, Niger State, Nigeria
[c] Department of Chemistry, Nile University of Nigeria, Abuja, Airport Road, Jabi, Abuja, Nigeria
[d] Nanotechnology Research Group, Africa Centre of Excellence for Mycotoxin and Food Safety, Federal University of Technology, PMB 65, Bosso, Minna, Niger State, Nigeria
[e] Department of Engineering Technology and Industrial Distribution, Texas A&M University, College Station, TX 77843, USA
[f] Department of Chemistry, University of the Western Cape, Robert Sobukwe, Rd, Private Bag X17, Bellville 7535, Cape Town, South Africa
[g] Department of Physics and Astronomy, College of Science, King Saud University, P.O. Box 2455, Riyadh 11451, Saudi Arabia
[h] Department of Chemistry, College of Sciences, King Saud University, Riyadh 11451, Saudi Arabia
[i] School of Geography and Environmental Sciences, University of the Witwatersrand, Private Bag X3, Wits 2050, Johannesburg, South Africa

ARTICLE INFO

Keywords:
Nanoparticles
Nanocomposite
Metal dopant
Photocatalytic activity
Box-Behnken Design Optimization
Toxicity test

ABSTRACT

Box-Behnken Design Optimization of the photocatalytic activity of the synthesized Na@Mg@Ti@$ZnWO_4$ nanocomposite at different mixing ratios for the degradation of malachite green in wastewater was investigated. The synthesized $ZnWO_4$-based nanomaterials were characterized using different analytical techniques. Optical analysis demonstrated a reduction in the band gap energy from 4.68 eV for $ZnWO_4$ to 2.08 eV for the doped $ZnWO_4$. HRTEM/HRSEM images revealed the formation of well-defined nanocrystals with distinct lattice fringes, while EDX confirmed the homogeneous distribution of dopants (Na, Mg, and Ti) on $ZnWO_4$. The XRD analysis showed that the incorporation of the dopant did not change the phase of $ZnWO_4$. In $ZnWO_4$, XPS revealed electron sharing between 3 s (Na and Mg) and 3d (Ti) dopants. The host and doped $ZnWO_4$ surface areas increased from 24.74 m^2/g to 156.93 m^2/g. Compared to the SPCE/$ZnWO_4$/Na/Mg/Ti electrode, cyclic voltammetry analysis confirmed strong conductive properties. Maximum removal of 99.93 % malachite green (MG) from wastewater was achieved using catalyst load (0.7 g) ($ZnWO_4$@NaMgTi), contact time (35 min), and pH 12. Even after five repeated cycles, $ZnWO_4$ nanocomposite doped with 1 % Na, 1 % Mg, and 1 % Ti exhibited superior photocatalytic behavior than other $ZnWO_4$ nanoparticles. A toxicity test demonstrated that dyeing wastewater treated with $ZnWO_4$@NaMgTi nanocomposites supported aquatic life (juvenile fish) better than untreated dyeing wastewater, standard water of fish farming, and water treated with $ZnWO_4$ nanoparticles alone. The immobilization of $ZnWO_4$ with the dopants contributed to the enhanced photocatalytic and electrochemical performance.

1. Introduction

Recently, photocatalytic technology has emerged as a promising solution for the degradation of organic substances through the utilization of non-selective hydroxyl radicals (•OH) generated by photooxidation-reduction reactions [1–4]. Researchers have utilized various heterogeneous photocatalysts to break down organic dyes in wastewater under artificial and natural light sources [5]. Of all semiconductors photocatalyst nanostructured materials, $ZnWO_4$ nanoparticles have exceptional characteristics, such as high photocatalytic

* Corresponding author at: Department of Chemistry, Federal University of Technology, PMB 65, Minna, Niger State, Nigeria.
** Corresponding author.
E-mail addresses: jimohtijani@futminna.edu.ng (J.O. Tijani), aezzat@ksu.edu.sa (A.O. Ezzat).

https://doi.org/10.1016/j.inoche.2025.114012
Received 10 November 2024; Received in revised form 20 January 2025; Accepted 22 January 2025
Available online 31 January 2025

activity and stability in the ultraviolet region, ease of synthesis, good luminescent properties, non-toxicity, and low cost in the field of wastewater treatment [6–8].

$ZnWO_4$ nanoparticles exist in various phases, such as monoclinic wolframite, Sanmartinite, and anorthic (triclinic) structures, depending on the calcination temperature. These nanoparticles typically exhibit a space group of P2/c, with oxygen ions (O) surrounding the tungsten (W). $ZnWO_4$ nanoparticles have been produced through various methods, including hydrothermal synthesis, microwave reduction, microwave-assisted hydrothermal, solvothermal, sol–gel, precipitation, co-precipitation, and the green chemistry approach [9,10]. This study employed the sol–gel technique, which involves transforming a solution (sol) into a solid three-dimensional gel phase through transformation, hydrolysis, and condensation processes, resulting in a high-purity product and a narrow size distribution of nanoparticles at low temperatures for $ZnWO_4$ preparation.

$ZnWO_4$ exhibits a dual structure-scheelite-type tetragonal and wolframite-type monoclinic-based on the cation's ionic radius [11]; it is part of the tungstate family and has been widely utilized for years to mineralize organic pollutants under UV [12] and sunlight [13] exposure. On the other hand, $ZnWO_4$ nanoparticles display limited catalytic activity in the visible spectrum due to their wide band gap (ranging from 3.9 to 4.5 eV), resulting in swift recombination of electron-hole pairs, weak performance, and poor retrieval of the catalyst from water after use, thus hindering its practical applications [10].

Researchers have extensively investigated methods to enhance the $ZnWO_4$ semiconductor's photocatalytic activity for practical uses [10,14]. Various approaches have been explored, including surface modifications, metal or non-metal doping, sometimes co-doping, and even multiple doping. Transition element dopants like Mn^{2+} and Co^{2+} altered the host material's electronic structure and its modulating ability. Doping typically induces band gap adjustments in nanomaterials by shifting the positioning of Ec and band bending. Introducing metal dopants fills the intralayer gaps within the molecular structure, not the spaces between layers [3,4,15]. This process stabilizes the doped nanomaterial by engaging π electrons with the dopant within these gaps. Incorporating transition metal ions into the semiconductor can alter its optical absorption range from ultraviolet to visible light. Previous studies found that doping or co-doping of $ZnWO_4$ with metals improved the photocatalytic performance of the host catalyst by preventing electron and hole recombination; it suffers from problems of thermal stability and subsequent loss of the dopant(s) during the catalyst preparation [14,16]. The mono-doping of $ZnWO_4$ with transition and rare-earth metals such as Cr^{3+}, Mn^{2+}, Cu^{2+}, and La^{3+} and their photocatalytic performance have been reported [17,18]. In a different experiment, Eu^{3+}, Tb^{3+}, and Li^{+} were added separately to the surface of $ZnWO_4$ nanoparticles. However, XRD patterns showed that the doping process did not create any new phases [19]. Nonetheless, single-metal doping has the drawbacks of reduced quantum efficiency and thermal instability. Additionally, introducing both metals into the $ZnWO_4$ nanoparticles did not notably affect the final product's crystallinity.

One of the recent advances in the field of photocatalysis is the triple doping of semiconductor material with metals or non-metals, which would lead to simultaneous changes in electronic structure and the creation of new doping levels within the band gap region of $ZnWO_4$. Yadev et al. (2018) investigated $ZnWO_4$ nanocomposites infused with Tm^{3+}, Yb^{3+}, and Mg^{2+}. Their findings revealed that incorporating Mg^{2+} enhanced both the crystallinity and the intensity of absorption bands within the material. This addition also led to a decrease in the material's optical bandgap. Consequently, this reduced the recombination of these pairs by acting as trap centers. Dutta and Ravel [17] synthesized $ZnWO_4$ nanoparticles with a band gap of 3.21 eV. They observed that individually doping these nanoparticles resulted in notably lower band gaps. Notably, undoped $ZnWO_4$ exhibited poorer catalytic performance and degraded the MB organic dye for the longest time. Abubakar et al. [20] reported triple doping of $ZnWO_4$ nanoparticles with carbon, boron, and nitrogen. They found that the nanostructured material successfully removed malachite green from dyeing wastewater. The present work selected alkali (sodium, Na), alkali earth (magnesium, Mg), and transition (titanium, Ti) metals as dopants, expecting them to enhance the photocatalytic activity of $ZnWO_4$ nanostructures by generating oxygen, zinc, or tungsten vacancies through interactions between the s and d electrons of the selected dopants and the conduct or valence band of $ZnWO_4$ nanoparticles. Doping $ZnWO_4$ with Na, Mg, and Ti could enhance photocatalytic activity by increasing charge separation efficiency, structural stability and surface area, enabling better photocatalysis of dyes. These nanocomposites will extend the light absorption range into the visible spectrum, increasing photocatalytic performance under natural light, leading to faster degradation of organic dyes, reduced toxicity, and greater environmental compatibility. This innovative approach offers a sustainable solution for managing dyeing wastewater, addressing both pollution reduction and water reuse challenges effectively.

The dyeing industry widely employs Malachite Green (MG), a cationic dye, to dye leather, paper, and silk; however, degrading this organic dye into harmless compounds using conventional methods has proven to be challenging. Given the significant impacts of exposure to local dyeing wastewater, exploring alternative treatment methods for the mineralization of the organic pollutants found in such wastewater is crucial. This study reports, for the first time, the preparation of $ZnWO_4$ nanoparticles doped with Na, Mg, and Ti for degrading malachite green in dyeing wastewater. Additionally, a toxicity test was conducted on the treated wastewater using $ZnWO_4$@NaMgTi nanocomposites to evaluate their ability to support aquatic life. The process involved synthesizing $ZnWO_4$ nanoparticles via sol–gel methods, followed by doping $ZnWO_4$ with different amounts of Na, Mg, and Ti through wet impregnation techniques. The efficacy of these materials in degrading malachite green in dyeing wastewater was evaluated using photocatalytic technology, and toxicity tests were conducted on both untreated and treated water samples using juvenile fish. The potential for regenerating and reusing the $ZnWO_4$-based photocatalysts was also investigated.

2. Materials and methods

The following analytical-grade chemicals and reagents: zinc acetate dehydrate (99 %), sodium tungstate dehydrate (96.0 %), titanium (IV) isopropoxide (99.9 %), magnesium (II) nitrate hexahydrate (98.0 %), sodium hydroxide (99.9 %), and sodium chloride (99.5 %) were obtained from Sigma Aldrich and used without further purification. We collected the indigenous dyeing wastewater from Tudun Wada, Kaduna, 200 m from the dyeing points south of Kasuwan Bacci Kaduna, in January 2021. The samples were stored in plastic containers and then maintained at 4 °C in a refrigerator prior to analysis. Before the sample collection, the plastic containers were simultaneously rinsed with 10 % nitric acid and de-ionized water.

2.1. Synthesis of triple-doped $ZnWO_4$ nanoparticles with Na, Mg, and Ti

In this study, nanocomposites of $ZnWO_4$ doped with multiple metals were developed using a wet impregnation technique. The synthesis of $ZnWO_4$ nanoparticles via the sol–gel method had been previously reported [20]. The synthesis mixture was prepared by combining 25 cm^3 of 1 % NaCl solution, 1 % $Mg(NO_3)_2{\cdot}6H_2O$, and 1 % $Ti(OCH(CH_3)_2)_4$ solution (w/v) in a 1:1:1 ratio. The mixture was then added to a 250 cm^3 beaker along with 3 g of $ZnWO_4$ nanoparticles. The solution was agitated for a period of 3 h, followed by rinsing, drying at a temperature of 85 °C for the entire night, and finally being identified as $ZnWO_4$@-NaMgTi. The weight percentage ratio of each of the dopants (Na, Mg, and Ti) in the synthesis mixture varied in the following ratios: 1:1:1, 1:2:1, 1:1:2, and 2:1:1 (Na:Mg:Ti). The samples based on the mixing ratios were coded: $ZnWO_4$@1Na1Mg1Ti, $ZnWO_4$@1Na2Mg1Ti, $ZnWO_4$@1Na1Mg2Ti, and $ZnWO_4$@2Na1Mg1Ti.

2.2. Characterization of $ZnWO_4$-based nanocomposites

HRTEM (Zeiss Auriga) was used to examine the microstructure and morphology of the prepared nanocatalysts. HRSEM (Zeiss Auriga) coupled with EDS was used to determine the morphology of $ZnWO_4$ nanoparticles. The shape of $ZnWO_4$ nanoparticles was studied using HRSEM (Zeiss Auriga) along with EDS. Their pore size and surface area were measured using BET (NOVA4200e, Quantachrome UK), and the samples were degassed under nitrogen at 90 °C for 4 h. X-ray diffraction (Bruker D8 diffractometer) was employed for phase identification of the nanoparticles, recording diffractograms in the 2θ range of 15° to 80°, and the crystallite size was calculated using the Debye-Scherrer equation (1);

$$d = \frac{k\lambda}{\beta cos\theta} \quad (1)$$

The crystallite size (d) in nanometers was calculated using Eq. (1), where K is 0.94, λ is 0.1541 nm, θ is the half diffraction angle, and β is the full width at half maximum in radians [21]. FTIR (Perkin Elmer 750) was used to identify the functional groups in the synthesized nanoparticles, while photoluminescence spectra were recorded using a Horiba Nanolog Spectrophotometer (iHR320). The absorption wavelengths of the synthesized nanomaterials were determined with a Shimadzu UV–visible spectrophotometer 1800, which was also used to identify organic dyes in local dyeing wastewater through the scanning of 2 mL of aqueous samples from 200 to 800 nm at 50 nm/min. The amount of MG in wastewater was estimated following the Beer-Lambert law. The pHpzc values of the nanomaterial were performed using the method described by Uko et al. [22].

2.3. Optimization of the photocatalytic process using Box-Behnken design

The design expert V.6.0.6 software from Stat-Ease Inc., USA, was utilized to conduct response surface modeling, statistical analysis, and optimize the photocatalytic experiment. The photocatalytic efficiencies of synthesized $ZnWO_4$, $ZnWO_4$@1Na1Mg1Ti, $ZnWO_4$@1Na2Mg1Ti, $ZnWO_4$@1Na1Mg2Ti, and $ZnWO_4$@2Na1Mg1Ti were assessed for degrading MG in indigenous dyeing wastewater under visible-light exposure. Three parameters (catalyst dose in mg, contact time in minutes, and pH) for the degradation of MG from dyeing wastewater were optimized via response surface methodology. These parameters were chosen as independent variables, while the percentage removal of MG served as the response variable. Table 1 displays the ranges and levels of the independent variables for the photocatalysts. Using the Box-Behnken Design (BBD), 20 experimental runs were conducted to explore the combined effect of the three independent variables. Before the photocatalytic experiment, the mixture of indigenous dyeing water containing MG and nanocatalysts was kept in darkness for 1 h to establish the adsorption–desorption process. Each experiment was then carried out at room temperature: for run 1, 0.4 g of the nanocatalyst was suspended in 100 cm^3 of the wastewater in a 1 L photoreactor in the darkness, and the solution pH was adjusted to 3 using 0.5 M HCl. The mixture was stirred at the specified speed of 300 rpm, according to Table 1. Following this, it was exposed to natural sunlight, which had a daily intensity of 1.70 x 10–9 Lux units, or 252.93 W/cm^3, and stirred for an hour. Subsequently, 5 cm^3 samples of the wastewater were regularly taken every 60 min and filtered using Whatman No. 1 filter paper to eliminate any remnants of the photocatalyst. The absorbance of the remaining MG was measured at the 617 nm maximum wavelength via a UV–visible spectrophotometer. Other experimental runs were repeated for the undoped $ZnWO_4$, $ZnWO_4$@1Na1Mg1Ti, $ZnWO_4$@1Na2Mg1Ti, $ZnWO_4$@1Na1Mg2Ti, and $ZnWO_4$@2Na1Mg1Ti as displayed in (Tables 2). The percentage MG degraded by the nanocatalyst was calculated using Eq. (2);

$$\%\,\text{MG removed} = \frac{\text{Initial absorbance} - \text{Final absorbance}}{\text{Initial absorbance}} \times 100 \quad (2)$$

The percentage removal of Malachite green generated various at various experimental conditions for $ZnWO_4$, $ZnWO_4$@1Na1Mg1Ti, $ZnWO_4$@1Na2Mg1Ti, $ZnWO_4$@1Na1Mg2Ti, and $ZnWO_4$@2Na1Mg1Ti is shown in Table 3.

Table 1
Independent factors and their coded levels for $ZnWO_4$ based photocatalysts.

Independent Variables	Symbols	Range and level		
		Low (−1)	Middle (0)	High (+1)
Catalyst dose (mg)	A	0.1	0.4	0.7
Contact time (min)	B	10	35	60
	C	3	7.5	12

2.4. Toxicity test of untreated and treated dyeing wastewater

2.4.1. Juvenile fish collection, acclimatization and exposure

In April 2022, young fish, 8 weeks old, were purchased in bulk from the Federal College of Freshwater Fisheries Technology in New Bussa, Niger State. All animal procedures received approval from the Institutional Animal Care and Use Committee (CICUAL) of Universidad de los Andes, with protocol code C.FUA 19–004, and followed their guidelines rigorously. The fish were acclimated to fresh water for 48 h, different from their original water, and fed formulated feed three times daily. A net covered the container to ensure proper air circulation and prevent suffocation. Known volumes (5000 cm^3) of undiluted raw wastewater and wastewater treated with $ZnWO_4$ and $ZnWO_4$@1Na1Mg1Ti were independently measured into four calibrated 16 L plastic containers. The experiment involved introducing 20 active juvenile fish into containers covered with perforated nets. In another trial, aerated tap water was used as a control. Both groups were observed in the laboratory for 96 h to assess fish survival rates in untreated and treated dyeing wastewater. The experiment maintained consistent temperature, pH, and conductivity conditions in the wastewater. Fish were not fed during treatment but were monitored daily. Fish counts were recorded after the exposure period. Survival and death rates were analyzed using two-way ANOVA Eq. (3), and the data were presented as the mean standard error of the mean (SEM).

Table 2
BBD results for photodegradation of MG using $ZnWO_4$ nanoparticles alone.

Run	Experimental conditions			Percentage removal of MG (%)	
	A – Catalyst dose (mg)	B – contact time (min)	C – pH	Experimental	Predicted
1	0.4	60	3	**47.17**	**49.43**
2	0.1	35	12	18.41	17.64
3	0.7	35	12	19.13	23.19
4	0.1	10	7.5	28.19	32.45
5	0.4	35	7.5	37.61	37.74
6	0.1	35	3	41.75	39.88
7	0.4	60	12	20.94	24.57
8	0.4	10	12	32.53	33.40
9	0.7	35	3	48.62	59.39
10	0.7	10	7.5	45.94	42.86
11	0.7	60	7.5	43.55	47.02
12	0.4	10	3	46.45	48.76
13	0.1	60	7.5	25.29	28.37
14	0.4	35	7.5	37.04	37.04
15	0.4	60	3	32.70	62.70
16	0.7	35	12	39.65	39.65
17	0.4	35	7.5	38.00	38.00
18	0.4	35	7.5	37.90	37.90
19	0.4	10	3	33.23	33.23
20	0.4	35	7.5	37.52	37.52

Table 3
BBD with actual and predicated values for removal of dye using 1Na1Mg1Ti/$ZnWO_4$ (response 1), 2Na1Mg1Ti/$ZnWO_4$ (response 2), 1Na1Mg2Ti/$ZnWO_4$ (response 3), and 1Na2Mg1Ti/$ZnWO_4$ (response 4).

	Factor 1	Factor 2	Factor 3	Response 1		Response 2		Response 3		Response 4	
Run	A:Dose	B:Contact time	C:pH	Actual	Predicted	Actual	Predicted	Actual	Predicted	Actual	Predicted
1	0.4	60	12	71.13	69.78	63.44	64.24	65.02	63.83	69.01	67.99
2	0.1	60	7.5	41.49	41.25	38.14	36.11	41.49	41.16	39.65	39.24
3	0.7	60	7.5	98.07	99.14	**98.07**	**97.12**	98.07	99.05	93.59	93.92
4	0.7	35	3	95.38	93.80	95.38	94.14	95.38	93.86	89.53	88.1
5	0.4	35	7.5	66.67	67.34	62.75	61.52	66.67	64.27	64.26	65.17
6	0.1	35	12	42.31	43.89	38.97	40.21	42.31	43.83	41.11	42.54
7	0.4	35	7.5	66.05	67.34	58.13	61.52	60.34	64.27	62.33	65.17
8	0.1	35	3	38.56	38.28	36.55	36.40	38.56	38.35	37.44	36.75
9	0.4	35	7.5	68.01	67.34	60.23	61.52	66.25	64.27	65.43	65.17
10	0.4	35	7.5	67.54	67.34	62.60	61.52	63.11	64.27	64.83	65.17
11	0.4	10	12	70.26	69.75	67.09	64.91	66.21	65.67	68.24	67.14
12	0.1	10	7.5	45.10	44.03	40.44	41.38	45.10	44.12	42.13	41.8
13	0.7	10	7.5	97.45	97.69	88.04	90.07	97.45	97.78	90.32	90.73
14	0.4	35	7.5	67.04	67.34	62.11	61.52	64.60	64.27	66.71	65.17
15	0.4	60	3	62.70	63.21	62.70	64.88	58.54	59.08	60.11	61.21
16	0.7	35	12	**99.65**	**99.93**	92.02	92.17	**99.65**	**99.86**	**94.12**	**94.81**
17	0.4	35	7.5	68.00	67.34	63.07	61.52	65.03	64.27	66.75	65.17
18	0.4	35	7.5	67.90	67.34	62.22	61.52	64.92	64.27	66.02	65.17
19	0.4	10	3	63.23	64.58	63.23	62.43	57.73	58.92	60.41	61.43
20	0.4	35	7.5	67.52	67.34	61.05	61.52	63.26	64.27	65.03	65.17

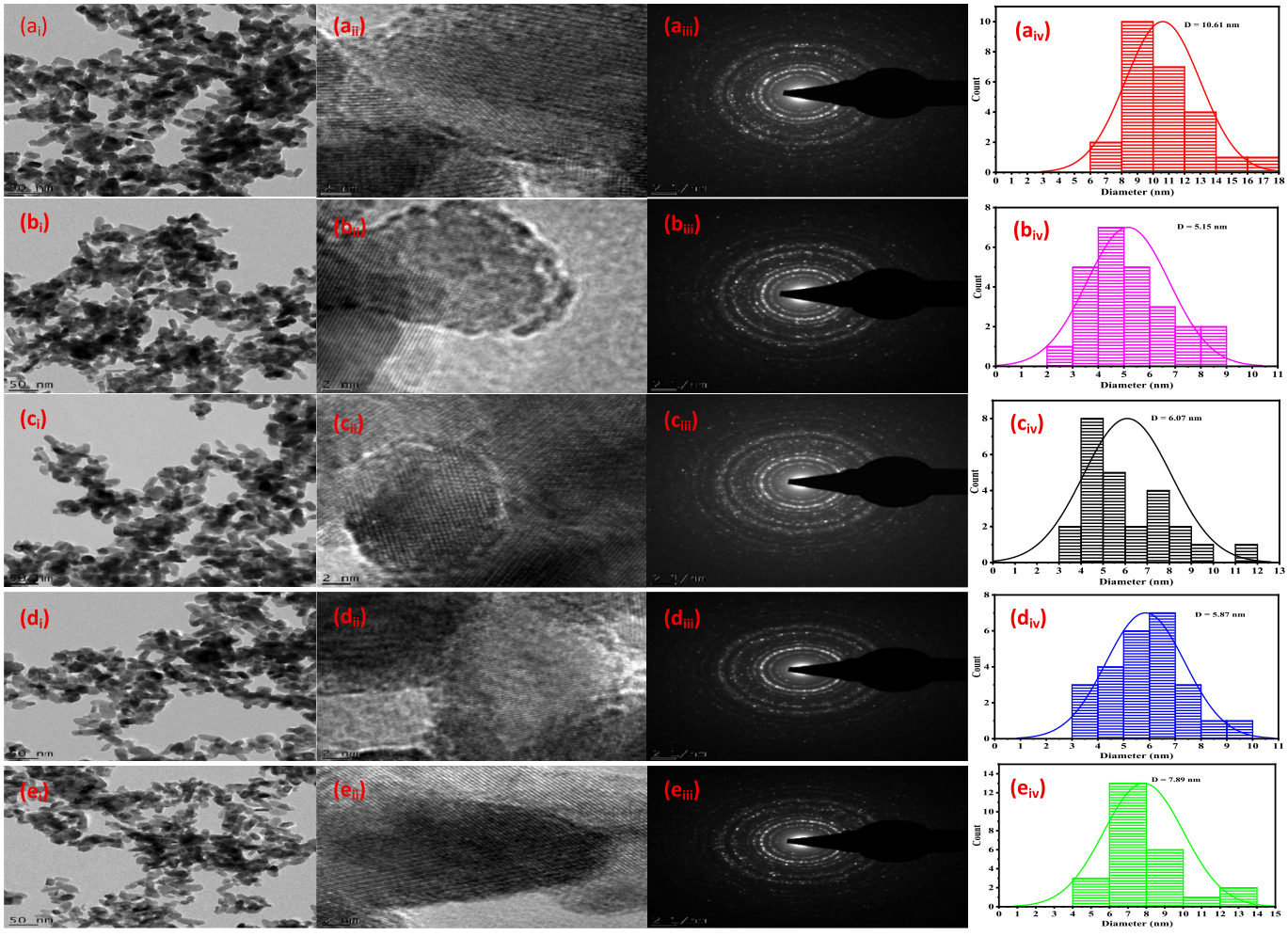

Fig. 1. (a-d). High and low magnification of HRTEM, SAED images and size distributions of $ZnWO_4$, 1Na1Mg1Ti, 1Na1Mg2Ti, 1Na2Mg1Ti and 2Na1Mg1Ti triple doped $ZnWO_4$ composites.

$$\text{Survival rate}\,(\%) = \frac{\text{Number of fish survived}}{\text{Total number of fish grown}} \times 100 \quad (3)$$

2.4.2. Regeneration study

The reusability of $ZnWO_4$ nanoparticles and $ZnWO_4$@1Na1Mg1Ti was evaluated by treating the used nanocatalysts with 0.5 M HNO_3. This treatment involved mixing the nanocatalysts with HNO3 in a flask, shaking for 30 min at room temperature, and then allowing the nanomaterials to absorb MG and form a complex nitrate. The nanocatalysts were subsequently washed with de-ionized water until the pH was 7, dried at 105 °C for 48 h, and calcined at 450 °C for 3 h. The treated nanomaterials were then used for four more cycles of adsorption–desorption in dyeing wastewater under conditions of pH 3, 60 min contact time, and 0.4 g catalyst dose. The reused catalysts were characterized using FTIR and XRD techniques.

3. Results and discussion

3.1. HRTEM and SAED of Na, Mg and Ti triple doped $ZnWO_4$ nanocomposites

High-resolution transmission electron microscopy (HRTEM) micrographs at high (2 nm) and low (50 nm) magnification and SAED images of the synthesized Na, Mg, and Ti-doped $ZnWO_4$ nanoparticles are

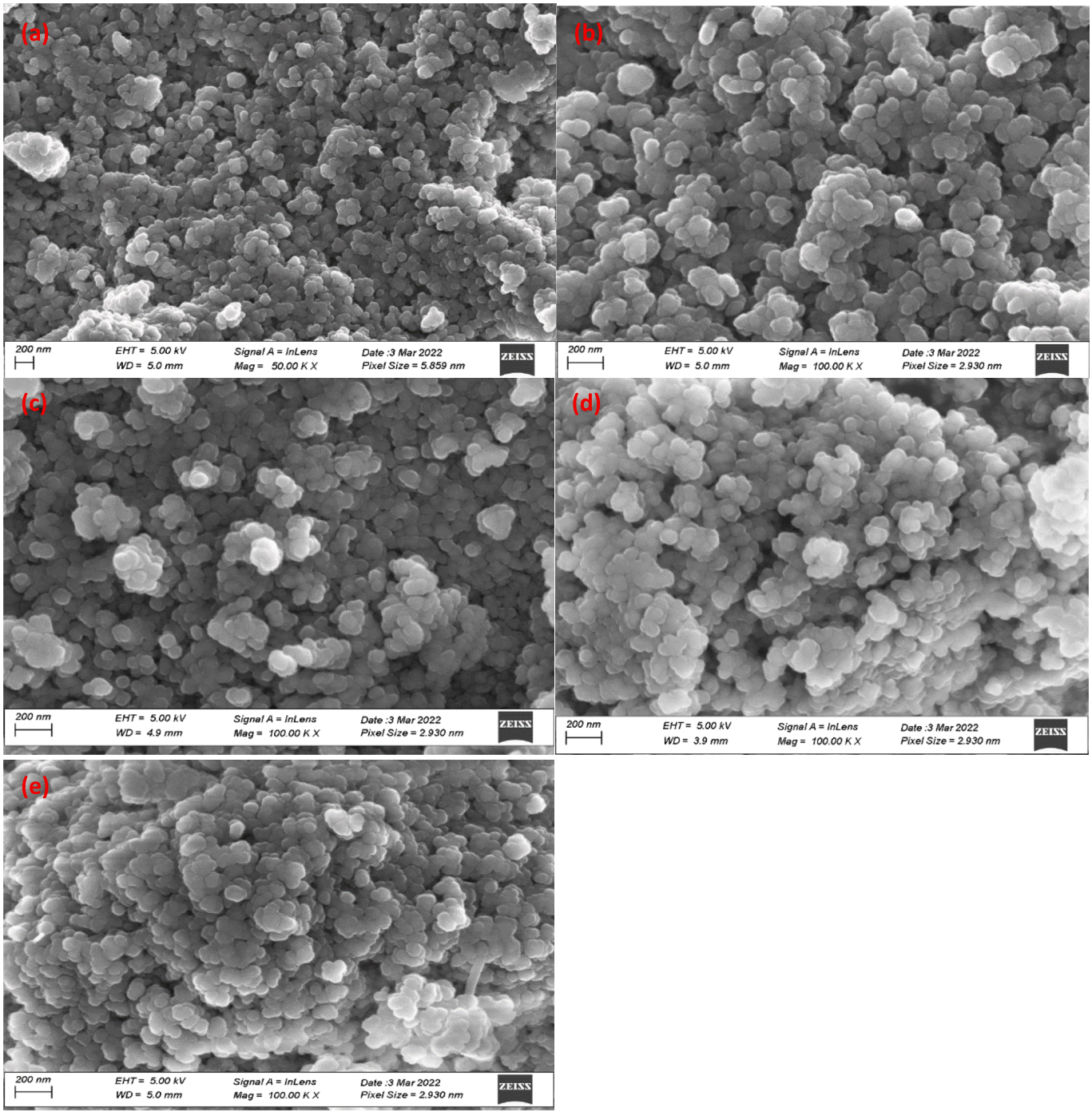

Fig. 2. (a-d). HRSEM micrographs of (a) undoped $ZnWO_4$ and triple doped $ZnWO_4$ nanocomposites (b) 1Na1Mg1Ti, (c) 2Na1Mg1Ti, (d) 1Na2Mg1Ti and (e) 1Na1Mg2Ti.

shown in Fig. 1. (a-d). The micrographs illustrate evenly distributed agglomerated spherical particles of $ZnWO_4$ arranged in an irregular fashion, irrespective of the dopant, as seen in Fig. 1(a-c). This suggests successful doping of the metals onto the $ZnWO_4$, as the darker spots portions of the heterojunctions among the metallic components [12,16]. The slight change in morphology and agglomeration rate for some of the particles may be due to the incorporation of different amounts of Na, Mg, and Ti ions into the host lattice of $ZnWO_4$. The selected area electron diffraction (SAED) patterns and low magnification HRTEM images of the multiple doped $ZnWO_4$ nanocomposites presented revealed the presence of bright spots and lattice fringes, which clearly indicate relatively high crystallinity for the Na, Mg, and Ti-doped $ZnWO_4$ nanocomposites. However, the lattice fringes were clearer and less distorted when 1Na1Mg1Ti was added to the $ZnWO_4$ nanoparticles. This means that most of the Na, Mg, and Ti ions were trapped inside the $ZnWO_4$ framework. Furthermore, the d-spacing in the HRTEM micrograph also aligned well with the d-spacing calculated from the XRD patterns. The SAED pattern confirmed the prepared material is well-crystallized nanoparticles and grown along the [021] plane direction [23]. The SAED micrographs of the multiple-doped $ZnWO_4$ nanomaterials revealed whitish spots around the concentric rings; this shows that these nanomaterials are polycrystalline, as well as that the crystal planes (021), (1 1 1), (1 1 0) and (1 0 0) aligned with the diffraction rings on the SAED images. The crystallinity corroborates with the XRD patterns for each nanocomposite material and the trend of particle sizes, as presented in Fig. 1(a_{iv}-e_{iv}), commensurate with the crystalline sizes from the XRD results. Overall, the SAED micrographs of nanomaterials analyzed show that they are highly polycrystalline in nature, irrespective of the dopant [24]. The incorporation of Na, Mg, and Ti undoubtedly led to some distortions in the lattice fringes of $ZnWO_4$, resulting in an increase in defects [25]. The SAED images reveal that the multiple-doped $ZnWO_4$ nanoparticles exhibit more dots in their rings than the mono-doped $ZnWO_4$ nanoparticles. This is because these dopant ions are impurities on the surface or lattice fringes of the nanoparticles, increase the surface roughness and surface area, and make the photocatalyst more effective than undoped $ZnWO_4$.

3.2. HRSEM analysis of triple metals doped $ZnWO_4$ nanocomposites

The surface morphologies of the undoped $ZnWO_4$ and triple metal-doped $ZnWO_4$ nanocomposites were examined using the HRSEM technique, and the micrographs are shown in Fig. 2. HRSEM analysis of the nanocomposite materials was carried out, and from the results obtained, the nanocomposites appeared to have more defined morphologies compared to the morphology before doping. This is because the dopants have successfully attached to the surface of the nanoparticles.

The HRSEM micrographs of the prepared multiple metal-doped $ZnWO_4$ nanocomposite materials revealed a spherical morphology just like the undoped $ZnWO_4$ nanoparticles, implying that loading the dopants did not cause significant distortions or phase changes in the $ZnWO_4$ nanoparticles [25]. It appears, however, that the nanocomposite materials were more compacted than the undoped $ZnWO_4$ nanoparticles (Fig. 2a). This difference in the HRSEM images in Fig. 2(b-e) may be due to the nature of the dopant, its ionic size, and its atomic size. Fig. 2(c and d), representing 2Na1Mg1Ti and 1Na2Mg1Ti, where Na^+ and Mg^{2+} dopant ions are double, respectively, showed more compacted nanocomposite materials because the two metals have the largest ionic radii at 1.06 Å and 0.72 Å respectively. Hence, doubling their concentration means that there were more of the larger dopant ions on the lattice of the $ZnWO_4$ material. This resulted in the displacement of O^{2+} and a reduction of the crystallite size compared to the undoped crystallite. This may be due to the existence of a synergetic or cooperative effect among the dopant ions on the surface of the material, and 1Na1Mg1Ti and 1Na1Mg2Ti multiple metal doped $ZnWO_4$ have a smaller crystallite size [23].

3.3. EDS analysis of multiple doped $ZnWO_4$ nanocomposites

Fig. S1(a-b) presents the EDS analysis for the $ZnWO_4$ nanoparticles multiple-doped with metals (Na, Mg, and Ti). For the multiple doped $ZnWO_4$ nanocomposites doped using 1Na1Mg1Ti, as seen in Fig. S1(a), the EDS patterns revealed the presence of the following major elements with their atomic percentages: Zn (35.56 %), W (33.19 %), O (17.33 %), Na (1.09 %), Mg (1.05 %), Ti (5.26 %) and 4.6 % C. The EDS pattern in Fig. S1(b) for $ZnWO_4$ nanocomposites multiple doped with 1 % Na, 2 % Mg, and 1 % Ti contained the dominant elements and their corresponding atomic percentages: 22.78 % Zn, 7.63 % W, 42.35 % O, 2.58 % Na, 5.23 % Mg, 6.9 % Ti, and 12.53 % C. Fig. S1(c) displays the elemental composition of $ZnWO_4$ nanocomposites doped with 1 % Na, 1 % Mg, and 2 % Ti. It shows the presence of the following elements, along with their corresponding atomic percentages: 25.99 % Zn, 19.33 % W, 44.86 % O, 2.31 % Na, 2.13 % Mg, and 4.38 % Ti. Fig. S1(d), which is a $ZnWO_4$ nanocomposite doped with 2 % Na,1 % Mg, and 1 % Ti, revealed the presence of the following elements: 39.91 % Zn, 37.63 % W, 14.90 % O, 3.95 % Na, 1.17 % Mg, and 2.44 % Ti. The EDS patterns for all the samples analyzed confirmed the presence of elements (dopant) of interest, which implies successful doping and the formation of 1Na1Mg1Ti, 1Na1Mg2Ti, 1Na2Mg1Ti, and 2Na1Mg1Ti doped $ZnWO_4$ nanocomposites.

3.4. XRD analysis of multiple doped $ZnWO_4$ nanocomposites

The phase structure of the $ZnWO_4$ nanocomposites multiple-doped with Na, Mg, and Ti with different molar ratios (1:1:1, 1:2:1, 1:1:2, 2:1:1) was determined using XRD, and the corresponding spectra obtained are displayed in Fig. 3. The phase of all multiple doped $ZnWO_4$ nanocomposites obtained was monoclinic with JCPDS No. 15–0554 and a space group of p2/c for this sample [17]. For the multiple metal-doped $ZnWO_4$ nanocomposites, the characteristic prominent diffraction peaks obtained were located at 2θ values of 18.90°, 24.57°, 30.47°, 36.31°, 41.14°, 54.26°, 61.65°, and 64.20°. This corresponds to the following miller indices: (100), (110), (111), (021), (121), (202), (113), and (311).

The average crystallite sizes calculated using Debye-Scherer are 4.22 nm, 6.67 nm, 6.44 nm and 4.95 nm, for 1Na1Mg1Ti, 2Na1Mg1Ti, 1Na2Mg1Ti, and 1Na1Mg2Ti multiple doped $ZnWO_4$ nanocomposite, respectively. Furthermore, the difference in crystallite sizes of the multiple doped nanocomposites may be linked to nucleation and growth kinetics [25]. This decrease in crystallite size with multiple doping suggests that the growth of the $ZnWO_4$ nanoparticles was suppressed by the three dopant ions on the sites of the host lattice, creating more nucleation sites [26]. The enhanced properties of the multiple doped nanocomposites may be linked to the combined effects of the orbital electrons of 3 s Na^+, 3 s Mg^{2+}, and 3d Ti^{4+} ions, which together displaced Zn^{2+} and W^{6+} and then coordinated with WO^{4+} to form Na_2WO_4, $MgWO_4$, and $TiZnO_3$ for vacancy compensation. This is because Na^+ has much larger ionic radii (1.06 Å) than Ti^{4+} (0.605 Å) and Mg^{2+} (0.23 Å) and an increase in the concentration of the Na^+ ions increased the chances of successful doping and further enhanced the properties of $ZnWO_4$ nanoparticles. Thus, the successful displacement of Zn^{2+} and W^{6+} through doping resulted in a reduction in the overall crystallite size of the material, which was initially 14.86 nm [27]. It is believed that Na^+ diffused onto the $ZnWO_4$ lattice via electrostatic attraction. Despite being the largest cation, the diffusion rate was much easier for Mg^{2+} with a smaller ionic radius, whereas Ti^{4+} with a slightly smaller ionic radius displaced W^{6+}. The combined effects of the Na^+, Mg^{2+}, and Ti^{4+} ions have enhanced the properties of the multiple doped nanocomposites. The 3 s ions of Na^+ and Mg^{2+} displaced Zn^{2+} and coordinated with W^{6+}, while the Ti^{4+} 3d ion displaced W^{6+} and coordinated with Zn-O for vacancy compensation. The displacement of ions that occurred by way of doping led to a reduction in the overall crystallite size of the material, which was initially 14.86 nm [27]. Generally, it was noticed that multiple doping with metals gave rise to the formation of

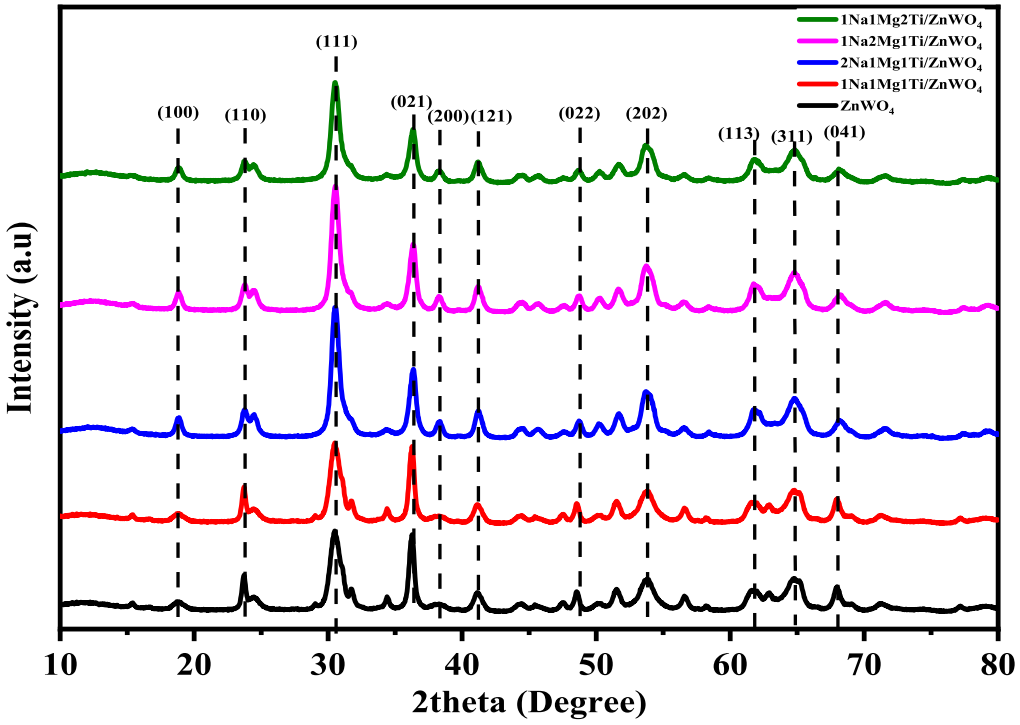

Fig. 3. X-ray diffraction patterns for triple metals doped $ZnWO_4$ nanocomposites prepared using different mixing ratio.

new diffraction peaks due to an increase in the number of substitutes (dopants), which caused a structural phase transition in the crystal lattice of the host material. For all the materials analyzed, the diffraction peak with miller index (1 0 0) at 2 theta values of 30.47° became more prominent, while the peaks at 2θ values of 31.26° shifted from (020) to 30.47° (1 1 1), and the one at 36.77° (120) shifted to 36.31° (021). The peak at 2θ value of 56.63° (202) shifted from 52.55° (122) and the peak at 64.35° (311), shifted from 65.51° (023). Generally, the introduction of foreign metallic impurities onto a material's surface causes these shifts or changes in orientation, altering the peaks and influencing other properties. A slight variation in the peaks observed was ascribed to the increased ionic strength and charged chemical potential of the crystal facets of the nanomaterials as the concentration of the dopants varied [28].

3.5. Textural properties of the undoped and doped nanocomposities

Table S1 presents the textural properties of nanocomposites, while Fig. 4 illustrates their corresponding adsorption–desorption curves. The undoped $ZnWO_4$ nanomaterials had a BET surface area of 4.7399 m^2/g, an average pore size of 0.0059 cm^3/g, and a total pore volume of 4.9630 nm. Table S1 showed that the triple doping effect significantly increased the surface area of the $ZnWO_4$ nanomaterials. These materials exist at the micrometric scale, indicating mesoporosity due to accumulated pore voids [25]. According to IUPAC, all multiple-doped nanomaterials exhibited a type IV isotherm with an H1-type hysteresis loop, indicating a predominance of mesoporosity. The surface area of the metal-doped nanomaterials increased in the following order: $ZnWO_4$ < $ZnWO_4$@2-Na1Mg1Ti < $ZnWO_4$@1Na2Mg1Ti < $ZnWO_4$@1Na1Mg2Ti < $ZnWO_4$@1Na1Mg1Ti, with a similar order observed for pore sizes. The highest increase in surface area (156.9256 m^2/g), pore volume (0.224 cm^3/g), and pore size (21.96 nm) was found in $ZnWO_4$ doped with 1 % each of Na, Mg, and Ti. The stacking of Na, Mg, and Ti particles on the $ZnWO_4$ surface may likely be responsible for this improvement. The increase in mesoporosity is attributed to the displacement and substitution of O^{2-} with Na^+, Mg^{2+}, and Ti^{4+} ions [29]. At high relative pressure, dopant ions expanded the pores and formed heterojunctions with multiple metal doping [23]. Variations in the surface areas of triple-doped nanomaterials may result from the dispersion of dopant ions on the $ZnWO_4$ surface [30].

3.6. XPS analysis of multiple doped $ZnWO_4$ nanocomposites

XPS analysis was carried out to determine the composition and chemical states in each of the elements present in the synthesized $ZnWO_4$ and 1Na1Mg1Ti doped $ZnWO_4$ nanomaterials, as depicted in Fig. 5. Fig. 5 shows the general survey spectrum of the nanomaterials and confirms the presence of all the dominant elements and the valence states of Na, Mg, and Ti are + 1, 2+, and 4+, respectively, based on the number of electrons in their valence shells. Therefore, it is essential to examine the chemical states of all three metallic ions doped onto the $ZnWO_4$ nanoparticles.

Fig. 6 represents high-resolution XPS spectra of Zn (2p), which show two peaks at binding energies of 1042.93 eV and 1019.27 eV for the undoped $ZnWO_4$, 1042.93 eV and 1019.27 eV for 1Na1Mg1Ti doped $ZnWO_4$. These peaks belong to Zn $2p_{1/2}$ and Zn $2p_{3/2}$, indicating that Zn is present in the + 2-oxidation state. The reduction in the binding energies of Zn in 1Na1Mg1Ti doped $ZnWO_4$ compared to Zn in $ZnWO_4$ suggests partial substitution of Zn with Na, Mg, or Ti.

Doping introduced dopant ions onto the surface of the prepared nanoparticles, causing a shift of the bands to a lower energy level. The Na and Mg, known as alkali and alkaline earth metals, could induce shallow donor states, thus reducing the bandgap. Ti, with its variable oxidation states, could introduce mid-gap states, increasing electron-hole recombination or separation. These changes shift the conduction and valence bands, lowering the overall bandgap energy. The dopant-induced strain and defects can also distort the lattice, affecting the density of states and electronic transitions, thereby shifting the bands to lower energy levels. The doping also resulted in the coordination and formation of Na_2WO_4, $MgWO_4$, and $TiZnO_3$. The W (5p) peak (Fig. 6-W 5p and W 4f and W 4d), which overlapped with the W (4f) peak, was 9 times more intense than the 5p of low intensity. However, a small component due to the 5p3/2 was hidden in the big peak of the 4f. The binding energy differences for the overlapping of 5p and 4f are 35.60 eV

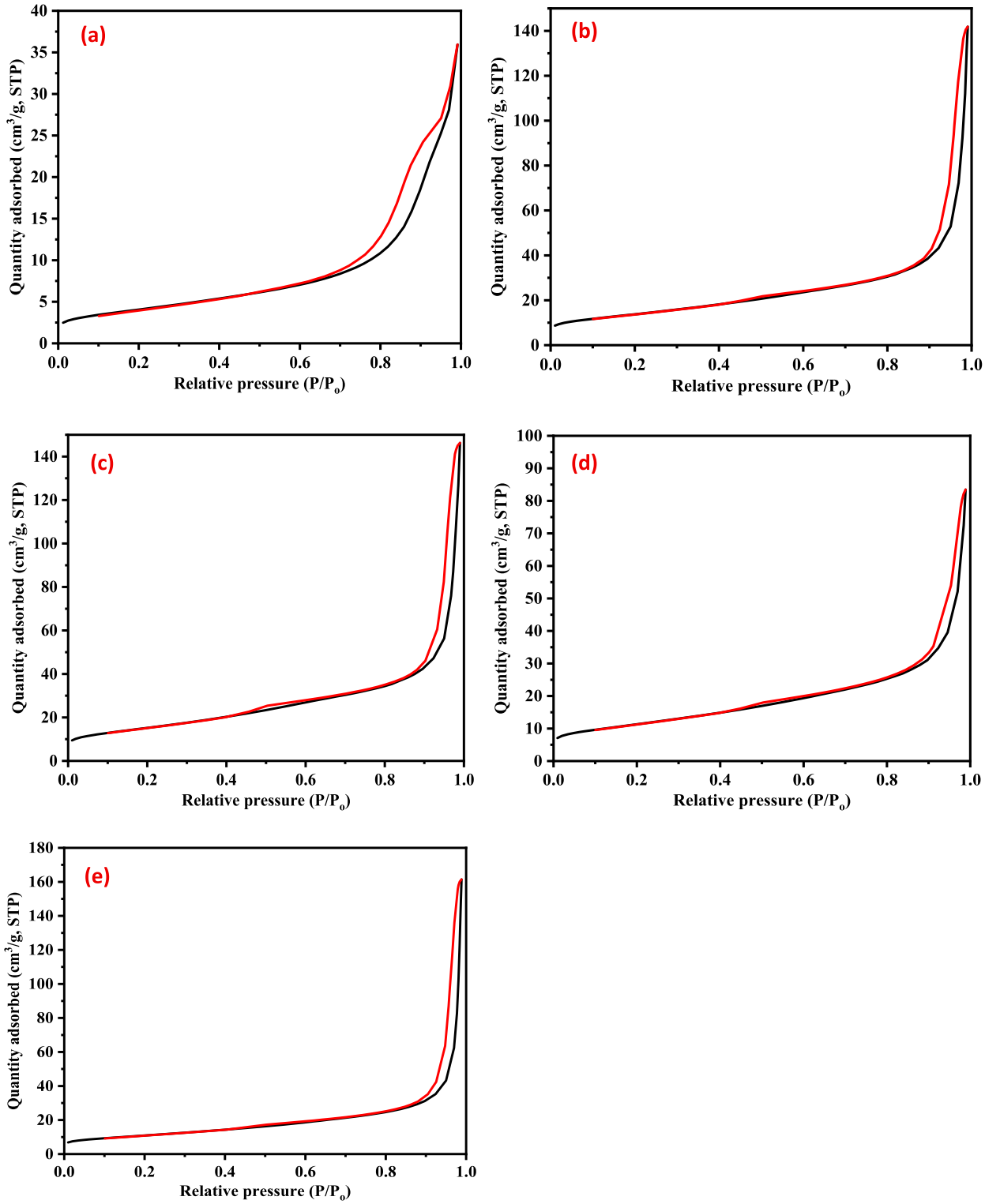

Fig. 4. Adsorption-desorption curves of (a) $ZnWO_4$, (b) 1Na1Mg1Ti, (c) 2Na1Mg1Ti, (d) 1Na2Mg1Ti and (e) 1Na1Mg2Ti.

and 35.87 eV for the $ZnWO_4$ and 1Na1Mg1Ti doped $ZnWO_4$ nanomaterials, respectively. These values corroborated the values obtained for $ZnWO_4$ as reported by Osotsi et al. [31], where a $ZnWO_4$-x nanomaterial with oxygen vacancy was synthesized and characterized.

Furthermore, to explain the origin of oxygen vacancies, high-resolution O (1 s) spectra are illustrated in Fig. 6-O 1 s. The asymmetric O 1 s peak at 528.87 eV for 1Na1Mg1Ti samples matches the oxygen coordination of Zn-O and W-O as well as surface chemisorbed oxygen [31]. The observed increase in peak intensity may be linked to the presence of O vacancies leading to the coordination and formation of Na_2WO_4, $MgWO_4$, and $TiZnO_3$. The formation of these compounds suggests that the W-O layer experienced the most impact while the Zn-O layer experienced the least, resulting in the formation of only one compound, $TiZnO_3$. The XPS spectra data demonstrates the successful formation of Na_2WO_4, $MgWO_4$, and $TiZnO_3$, indicating partial substitution of Zn in $ZnWO_4$ by Na and Mg and the transfer of excited electrons

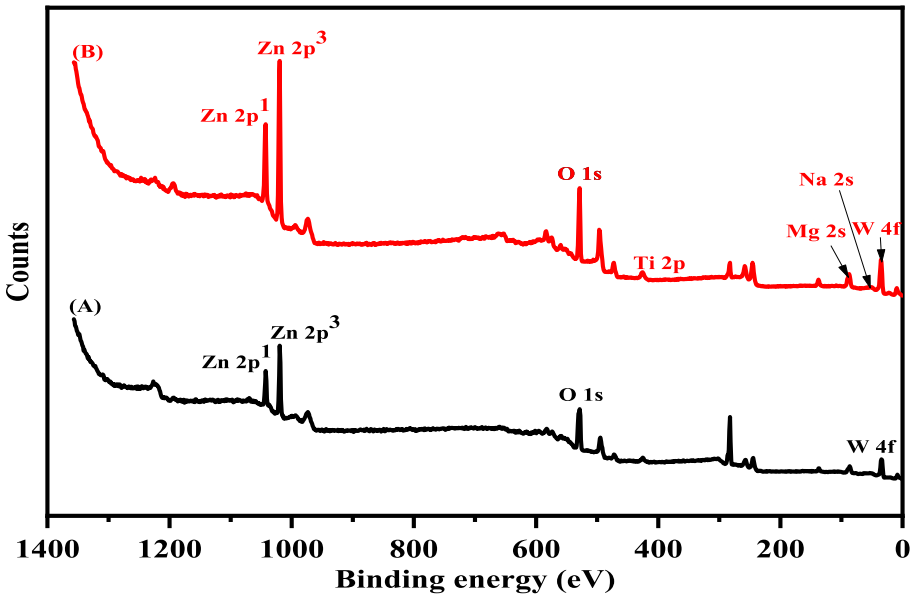

Fig. 5. XPS survey spectra of (A) $ZnWO_4$ nanoparticles (B) and 1Na1Mg1Ti doped $ZnWO_4$.

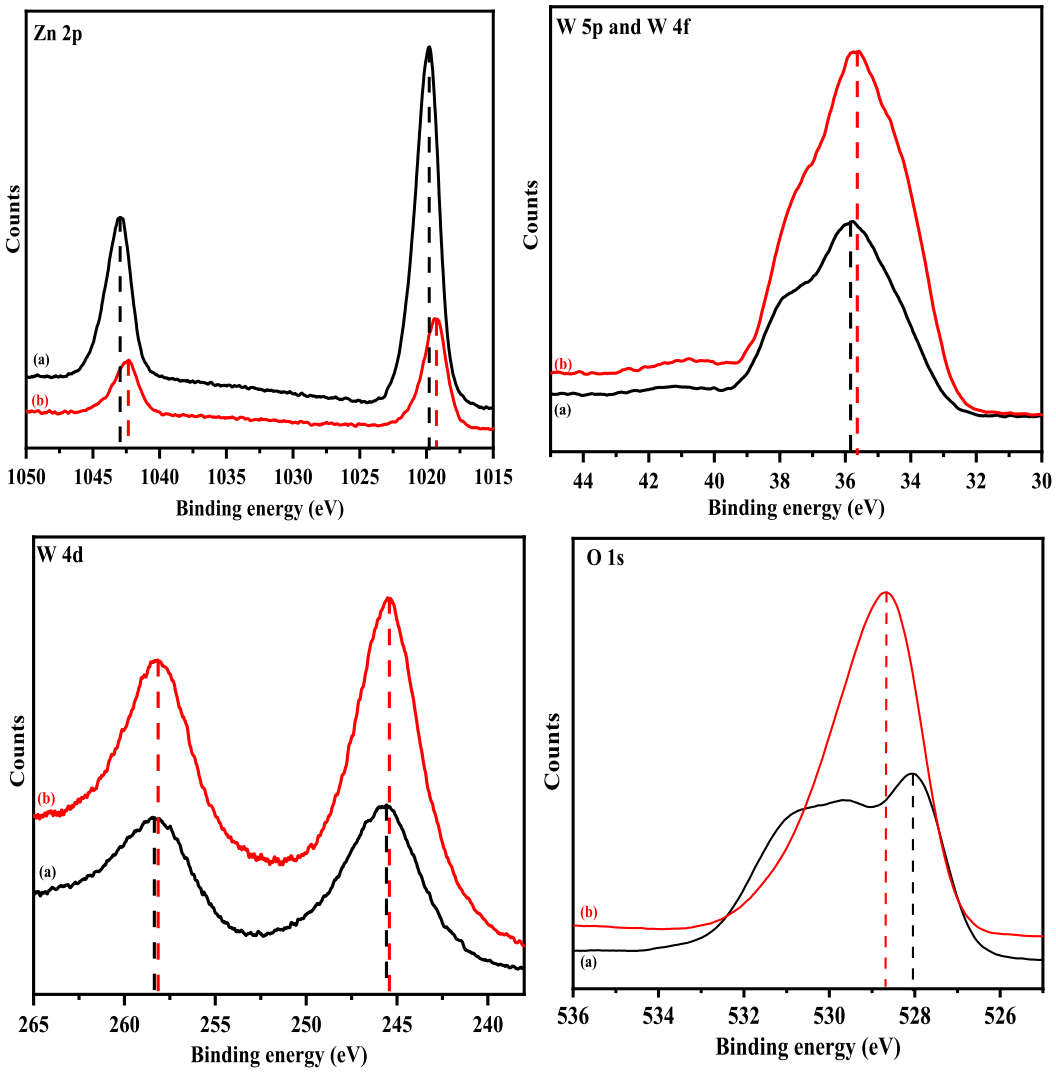

Fig. 6. High Resolution XPS survey of Zn 2p, W 5p and W 4f, W 4d and O 1 s orbital electrons in (A) $ZnWO_4$ nanoparticles and (B) 1Na1Mg1Ti doped $ZnWO_4$, respectively.

from $ZnWO_4$ to the dopants. In the case of $TiZnO_3$, the dopant species Ti was able to penetrate the $ZnWO_4$ framework, even though their ionic radiuses were different. This suggests that the host compound and Ti are interacting with each other. The XPS analysis revealed that the 3 s (Na and Mg) and 3d (Ti) dopants have different interactions with $ZnWO_4$ nanoparticles.

3.7. Electrochemical studies of $ZnWO_4$ and Na@Mg@Ti triple doped $ZnWO_4$ nanocomposite

The electrochemical investigation on $ZnWO_4$ (Fig. 7a) and $ZnWO_4$ doped with Na, Mg, and Ti (Fig. 7b) was conducted in 1 M KOH using cyclic voltammetry (CV) within the potential window of 0 to 0.6 V at 50 mV/s. Fig. 7 shows the CV profiles of unmodified and variously modified electrodes with 0.1 M KOH. The SPCE/$ZnWO_4$ electrode displays a consistent current response that increases with scan rates, indicating a notable decrease in electron mobility due to the material's non-conductivity. However, the electrodes SPCE/$ZnWO_4$/Na/Mg/Ti exhibit a high current response, suggesting a higher material conductivity, a larger electroactive surface area, and faster electron transfer compared to the other SPCE/$ZnWO_4$ electrodes. Additionally, the SPCE/$ZnWO_4$/Na/Mg/Ti composite displays a significantly increased capacitance current as compared to SPCE/$ZnWO_4$. As shown by these results, the enhanced SPCE/$ZnWO_4$/Na/Mg/Ti electrode exhibits strong conductive properties that promote higher charge transfer efficiency. The increase in current response and conductive properties may be due to the high intercalation rate and rearrangement of the $ZnWO_4$ lattice layer by the three metallic dopants.

3.8. UV–visible analysis

UV–visible spectroscopy was used to assess how doping influences

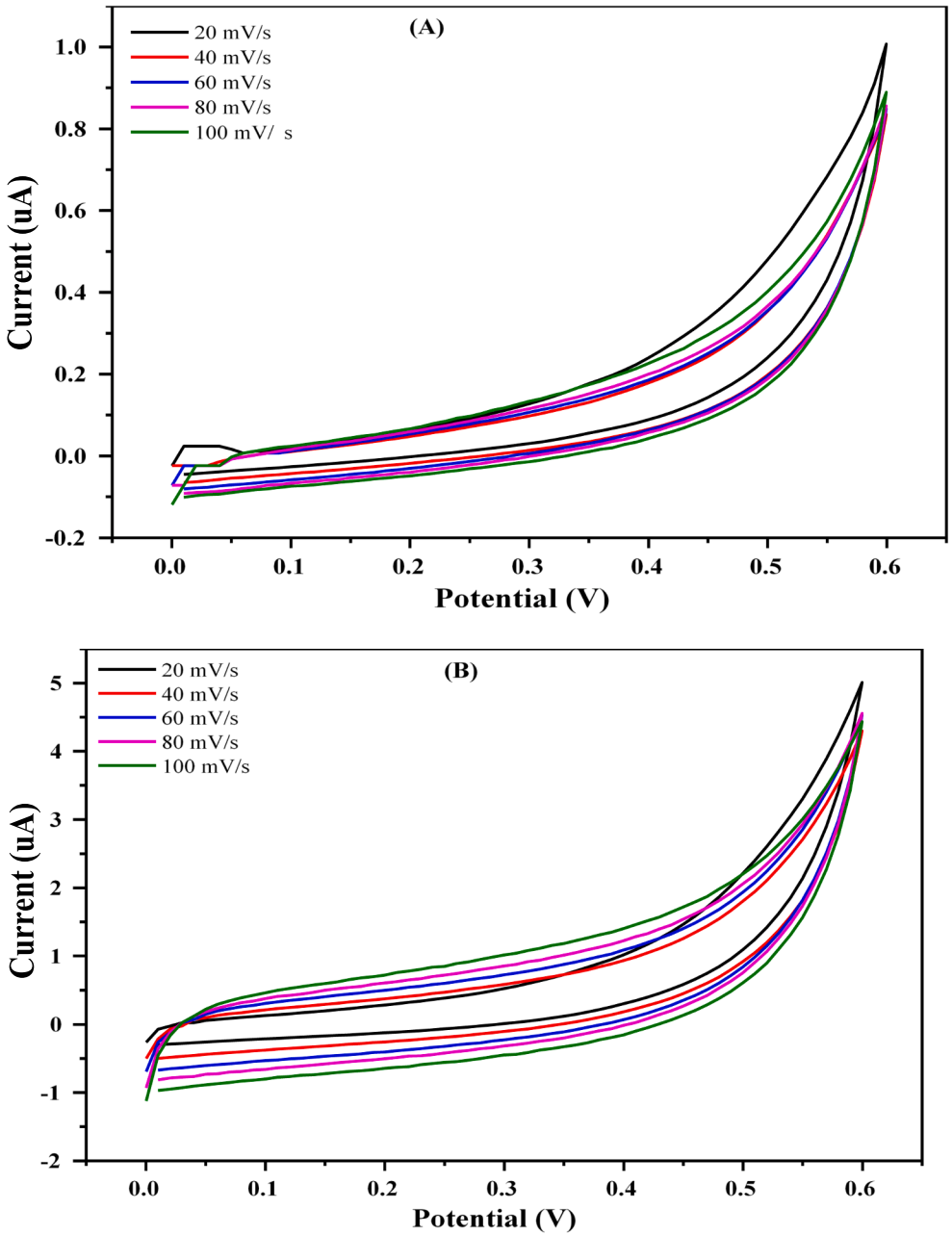

Fig. 7. Electrochemical studies behaviors of a) $ZnWO_4$ and b) 1Na1Mg1Ti doped $ZnWO_4$ at SPCE in 1 M KOH potential window 0 to 0.6 V at various scan rates.

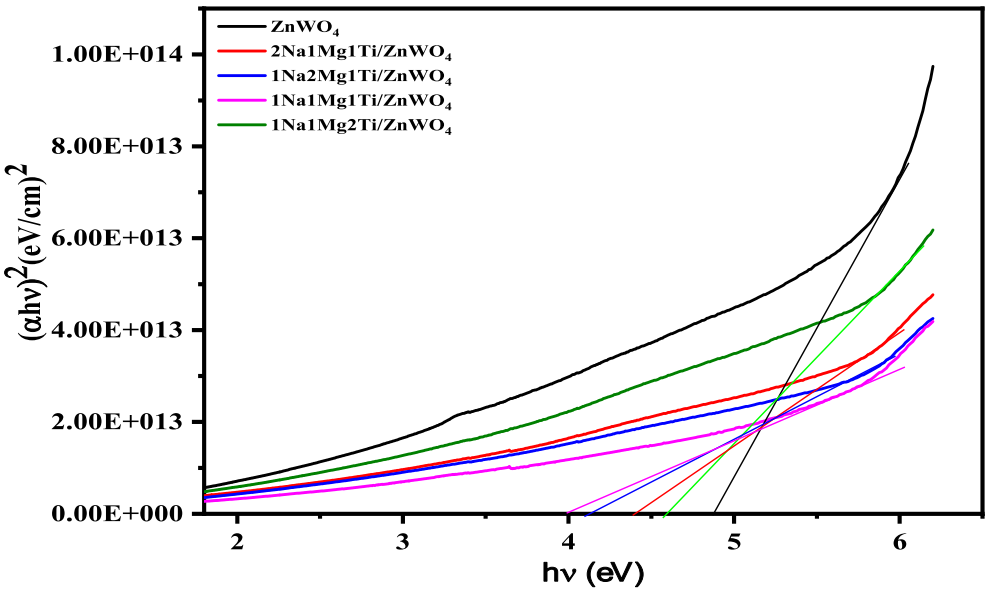

Fig. 8. Tauc's plot of the metals multiple doped $ZnWO_4$ nanoparticles.

the optical properties of synthesized $ZnWO_4$. Fig. 8 shows the Tauc spectra for both undoped and doped $ZnWO_4$ with 1 %Na1 %Mg1 %Ti, 2 %Na1 %Mg1 %Ti, 1 %Na2 %Mg1 %Ti, and 1 %Na1 %Mg2 %Ti. Doped materials exhibit a noticeable shift in their absorption edge towards longer wavelengths, known as a redshift. This shift is linked to charge transfer transitions between various dopant ions (Na, Mg, and Ti) and the valence or conducting band of $ZnWO_4$. Electron transfers occur between specific electron orbitals, indicating interactions between dopant orbitals and charge transitions within $ZnWO_4$ [32]. This wavelength shift suggests strong interactions between dopant orbitals and charge transitions within $ZnWO_4$. Post-doping, the bandgap energy significantly decreases, with the lowest value observed for 1 %Na1 %Mg1 %Ti-$ZnWO_4$. Multiple doping reduces the bandgap energy the most, especially when dopant concentrations are equal, as in 1 %Na1 %Mg1 % Ti-$ZnWO_4$. This suggests that the photocatalytic properties of 1Na1Mg1Ti (4.03 eV) are substantially enhanced in comparison to those of undoped materials, as observed by Geetha et al. [33,34].

3.9. Photoluminescence analysis of $ZnWO_4$ and multiple metal doped $ZnWO_4$

Fig. 9 displays PL spectra for $ZnWO_4$ and different metal rations doped $ZnWO_4$. The excitation wavelengths of Na/Mg/Ti and $ZnWO_4$ in the Na/Mg/Ti/$ZnWO_4$ nanocrystal were 315 nm, and the comparison of PL spectra is presented in Fig. 9. The crystallinity of $ZnWO_4$ significantly impacts its brightness. At the same time, surface oxygen vacancies and

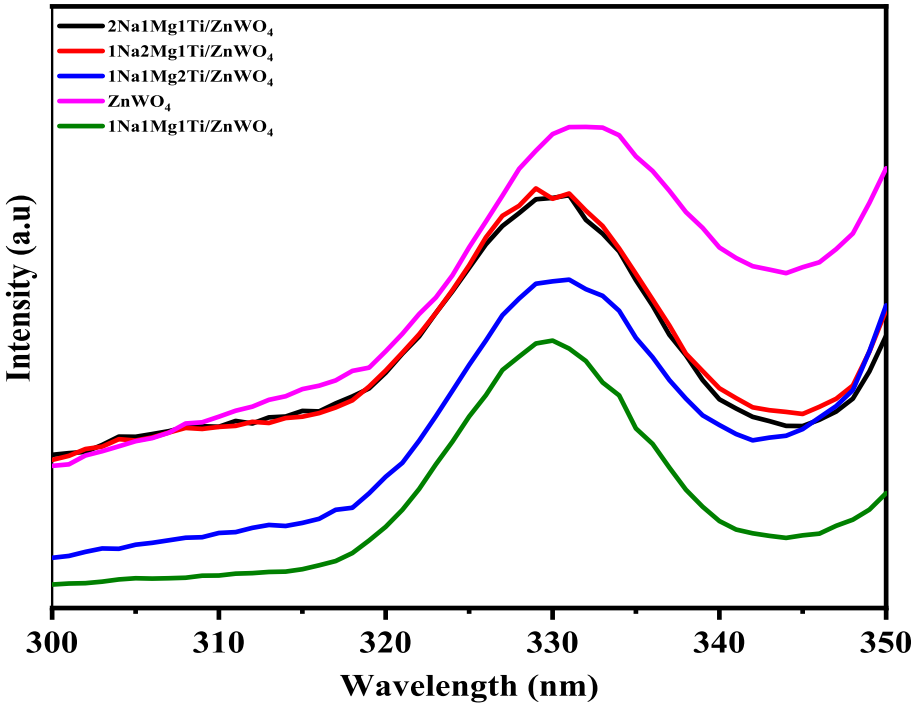

Fig. 9. PL spectra of $ZnWO_4$ and metals multiple doped $ZnWO_4$ nanoparticles.

defects are crucial for the excitonic photoluminescence of semiconductor nanoparticles. The emission of metal tungstate is due to charge transfer transitions within the WO_4 clusters, as shown in Fig. 4 (a). The emission peaks are 332.14, 328.90, 329.55, 330.95, and 330.72 nm for ZWO_4, and multiple metals (1Na1Mg1Ti, 1Na1Mg2Ti, 1Na2Mg1Ti, and 2Na1Mg1Ti) doped $ZnWO_4$, respectively. The high-intensity peak of $ZnWO_4$ is due to the recombination of photo-generated carriers in the $ZnWO_4$. For multiple metal dope $ZnWO_4$, the photoluminescence intensity peak dropped drastically, which indicates that the photogenerated carries were successfully separated in the composite. The presence of a dopant such as Mg may lead to a reduction in the PL intensity. This is due to the lower concentration of charge carriers and defects that can hinder radiative recombination. This suggests that the electron-hole recombination in the doped $ZnWO_4$ is less than that in bare $ZnWO_4$. The widely accepted view is that a lower PL intensity corresponds to a lower photo-carrier recombination rate and results in higher photocatalytic performance [35]. This further shows that the photocatalyst ($ZnWO_4$@1 %Na1 %Mg1 %Ti) has a higher photocatalytic activity for dye photodegradation than $ZnWO_4$.

3.10. Characterization of indigenous dyeing wastewater

3.10.1. Analysis of untreated dyeing wastewater

UV–visible spectroscopy was utilized to analyze the untreated dyeing wastewater in order to identify its organic dye content. Fig. S2 depicts the resulting adsorption spectrum. The adsorption bands detected at 210 nm, 332 nm, 445 nm, and 617 nm indicated the presence of MG. Previous research by Azimi et al. [36] identified a peak wavelength of 617 nm for MG, which was consistent with our findings for synthetic MG solution. These UV–visible analysis results informed the subsequent photocatalytic procedure.

3.10.2. Process optimization of the photocatalytic experiment

The design expert was utilized to conduct response surface modeling, statistical analysis, and optimize the photocatalytic experiment. Tables 2 and 3 present the experimental and predicted percentage removal of MG, illustrating the interplay of three parameters. The photocatalytic degradation experiment data underwent analysis of variance (ANOVA) (see Table S1). The study estimated the optimal values of combined parameters through a three-dimensional response surface analysis of independent and dependent variables.

Table 2 shows a maximum removal percentage of 49.43 % for $ZnWO_4$ under ideal conditions: Conversely, the model also indicated a minimum removal percentage of 37.64 %. To optimize MG dye removal in Indigenous dyeing wastewater using $ZnWO_4$, ANOVA highlighted the model's high significance, supported by an F-value of 13.45. There is only a 0.02 % probability that this F-value results from noise. The p-values, where < 0.05 indicates significance and > 0.1 suggests insignificance, confirmed the model's terms' significance. The predicted R^2 value (0.2148) suggests that, on average, using the overall mean might be a more effective predictor than the current model. However, employing a higher-order model could yield better predictions. Despite this, the adjusted R^2 value of 0.8550 indicates strong predictability. The adequate precision, with a ratio of 14.395, suggests a favorable signal-to-noise ratio, implying adequacy in the model, according to Arshad et al. [37]. Eq. (4) presents the polynomial relationship between the dependent variable—decolorization of malachite green in indigenous dyeing wastewater—and the independent variables: catalyst dose (A), contact time (B), and pH (C), represented in terms of coded factors.

$$Y = 98.51 + 15.02A - 0.42B - 8.38C + 0.37AB + 2.41AC - 0.0016BC - 24.40A^2 + 0.004B^2 + 0.30C^2 \quad (4)$$

In this study, Y represents the expected outcome, specifically the percentage of MG dye removed by the photocatalyst. A, B, and C represent encoded values relating to the catalyst dose, contact time, and pH, respectively, as independent variables. This equation evaluates the response based on varying levels of different factors. Analysis of the data in Table S2 (supplementary data) reveals that pH (C) had the most significant impact on MG removal efficiency, evident from its high F-value of 74.07. Additionally, the catalyst dose (A) had a notable impact, as indicated by its F-value of 28.77. However, contact time (B) had minimal effect on removal efficiency (%), with an F-value of 0.2654. Table S2 highlights an intriguing relationship between the predicted R^2 value and the adjusted R^2 values. The predicted value was negative, suggesting that the prediction deviated from the data trend in the chosen model. This indicates a less accurate prediction compared to the average value of the data, implying an inverse relationship between variables and reduced prediction precision as variable values increase [38,39]. The 3D response surfaces visually depict regression equations used to optimize reaction conditions involving catalyst dose, contact time, and pH for the removal of MG. The experimental conditions in Run 1 yielded the highest removal of MG dye based on the interactions among the three independent and dependent variables. Conversely, Run 2 showed the lowest removal efficiency.

In Fig. S4 (a), it was observed that the removal efficiency (%) of MG increased slightly as both the contact time and catalyst dose increased. This suggests a significant interaction, supported by the F-value of 28.77. In Fig. S4, a response surface showed that as pH increased, the removal efficiency decreased, while it increased with higher catalyst doses. However, the F-value for pH was 74.07, indicating less significance. Fig. S4(c) depicted the interaction between pH and contact time, revealing that increasing pH significantly reduced MG removal efficiency by $ZnWO_4$, whereas contact time had a marginal positive effect. This interaction had the least significant F-value at 0.2654 [40].

In the least efficient Run 2, the catalyst dose, contact time, and pH were set at 0.1, 35, and 12, respectively, with ranges of −1, 0, and + 1. Fig. S4(a) illustrates the influence of the interaction between contact time and catalyst dose. The study observed that longer contact times showed a slight improvement in removing MG, whereas higher catalyst doses significantly increased MG removal efficiency. This trend was associated with the F-values, ranking pH as the highest and contact time as the lowest, as depicted in Fig. S4(b). Interestingly, a rise in pH resulted in decreased MG removal efficiency, but an increase in catalyst dose consistently improved MG removal efficiency. The enhanced removal efficiency of MG by nanocatalysts can be attributed to electrostatic interactions between the anionic surface of the catalyst and the cationic surface of the dye, indicating a strong affinity between the adsorbate and the catalyst [38,39]. The increase in the dosage of catalysts leads to a higher number of adsorption sites, consequently improving MG removal efficiency [38,39]. Hanane et al. [40] observed that increasing pH levels led to a decrease in MG removal efficiency, while contact time had a minimal impact on efficiency.

Table 3 presents the removal of dye using composites of 1Na1Mg1Ti/$ZnWO_4$, 2Na1Mg1Ti/$ZnWO_4$, 1Na2Mg1Ti/$ZnWO_4$, and 1Na1Mg2Ti/$ZnWO_4$, under the influence of dose, contact time, and pH using BBD. Eq. (5) to (8) presents the Box-Behnken equations illustrating the effect of nanocomposites on the degradation of dyeing wastewater.

$$\%\,\text{Removal}\,(\textbf{Response1}) = 31.70 + 63.60A - 0.151B + 1.269C + 0.141AB + 0.0963AC + 0.003BC + 29.618A^2 + 0.00083B^2 - 0.0510C^2 \quad (5)$$

$$\%\,\text{Removal}\,(\textbf{Response2}) = 35.83 + 57.208A - 0.265B - 0.0247C + 0.411AB - 1.07AC - 0.0069BC + 34.819A^2 + 0.00243B^2 + 0.0532C^2 \quad (6)$$

$$\%\,\text{Removal}\,(\textbf{Response3}) = 29.66 + 27.94A + 0.0074B + 2.218C + 0.141AB + 0.0963AC - 0.0044BC + 74.194A^2 + 0.000676B^2 - 0.0975C^2 \quad (7)$$

$$\%\,\text{Removal}\,(\textbf{Response4}) = 29.04 + 67.87A - 0.0963B + 1.135C + 0.192AB + 0.17AC + 0.00238BC + 13.11A^2 + 0.000116B^2 - 0.0395C^2 \quad (8)$$

From Table 3, the actual and predicted values are closely aligned across most runs, indicating that the model used to predict dye removal is robust and reliable. For instance, in run 1, the predicted value (69.78 %) is very close to the actual value (71.13 %), suggesting the model accurately represents the experimental outcomes. The small deviations between actual and predicted values across various conditions indicate the model's high accuracy.

Higher doses generally correlate with higher dye removal efficiencies. For example, at a dose of 0.7 g, the actual dye removal efficiency is consistently high, demonstrating that increasing the dose enhances the catalytic activity, leading to better dye removal. The correlation between higher doses and increased dye removal efficiency in photocatalytic processes was supported by the findings of Jamal et al. [41], who demonstrated that increasing the ratio of a photocatalyst in a composite led to higher photocatalytic efficiency of dye removal. Longer contact times also appear to influence dye removal positively. For instance, at a contact time of 60 min, the dye removal efficiency is higher than at lower contact times. This trend is consistent with the kinetics of adsorption, where increased exposure time allows for greater interaction between the dye molecules and the active sites on the adsorbent or catalyst. For instance, Ghasemi et al. [42] demonstrated that the removal efficiency of methylene orange increased with additional layers of TiO_2 nanoparticles, indicating a direct relationship between the catalysts and dye removal efficiency. Similarly, Faroug [43] highlighted the efficient nature of photocatalytic degradation in breaking down dye molecules over extended periods, leading to the formation of less complex organic compounds and their eventual mineralization. The pH of the solution has a significant impact on the dye removal process. For example, at pH 12, the dye removal is high, likely due to the increased ionization of dye molecules and enhanced interaction with the catalyst surface at alkaline pH. Raliya et al. [44] found that at an alkaline pH, the photocatalytic efficiency increased, leading to higher dye removal rates, and also highlighted the use of hybrid nanocomposite photocatalysts for adsorptive-assisted photocatalytic dye removal, further underlining the precision and reliability of such systems.

All four models are significant (Tables S3 to S6), with very low p-values (< 0.0001), indicating that the quadratic models effectively describe the data. The R^2 values for all models are close to 1, indicating a strong fit. The R^2 values are 0.9976, 0.9930, 0.9930, and 0.9955 for responses 1, 2, 3, and 4, respectively. The adjusted and predicted R2 values are also high, confirming the models' fitness. The 3D response surface and contour plots are presented in Figs. S5 to S8 illustrates the response variable changes as a function of two independent variables, with the third variable held constant. Dose is the most significant factor across all models, with the highest F-values and very low p-values (< 0.0001). This suggests that the dose has the most substantial impact on dye removal efficiency. The sum of squares for dose is significantly higher than other factors, confirming its dominance in influencing the response. For instance, in the model for 1Na1Mg1Ti/$ZnWO_4$, the sum of squares for dose is 6221.14, which is considerably higher than the sum of squares for contact time (0.8778) and pH (68.91). Similarly, in the model for 1Na1Mg2Ti/$ZnWO_4$, the sum of squares for dose is 5368.03, affecting the contributions of other factors. Contact time has minimal impact on the removal efficiency across all models, as indicated by the very low sum of squares, low F-values, and high p-values (all above 0.05). This suggests that variations in contact time do not significantly affect the removal efficiency, making it the least influential factor among those considered. For example, in the model for 1Na1Mg2Ti/$ZnWO_4$, the sum of squares for contact time is only 0.1984, with a p-value of 0.7829, indicating no significant contribution. The pH factor is significant in most models, particularly in the model for 1Na2Mg1Ti/$ZnWO_4$, where it has a p-value of 0.0021 and an F-value of 16.97. The sum of squares for pH is also relatively high, indicating its importance in the removal process. However, its influence is less consistent across different models, with varying significance levels. In some models, like 2Na1Mg1Ti/$ZnWO_4$, the p-value for pH is not significant (0.5476), suggesting that pH may not always be a critical factor depending on the specific material combination.

Interactions (AB, AC, and BC) and quadratic terms (A^2, B^2, and C^2) have varying degrees of significance across the models. For instance, in the model for 2Na1Mg1Ti/$ZnWO_4$, the AB interaction is significant with a p-value of 0.0142, indicating a combined effect of dose and contact time on the removal efficiency. On the other hand, in the model for 1Na2Mg1Ti/$ZnWO_4$, the A^2 term is highly significant, with a p-value $<$ 0.0001, indicating a strong quadratic effect of dose on the response. The variation in significance across the models suggests that different material compositions interact differently with dose, contact time, and pH. The 1Na1Mg1Ti/$ZnWO_4$ nanocomposite has a high visible light photocatalytic performance (almost 100 %), indicating its potential for efficient dye degradation. The high surface area of the nanocomposite makes it suitable for catalyzing the degradation of dyes, highlighting its effectiveness in the photodegradation of dyeing wastewater. The dominance of dose in influencing removal efficiency is attributed to its direct impact on the availability of active sites for photocatalytic reaction, which is critical for the removal process. The lesser influence of contact time may indicate that equilibrium is reached quickly, and extending the contact time does not enhance removal efficiency. The varying significance of pH highlights its role in altering the surface charge of the materials and the ionization state of pollutants, affecting their interaction with the adsorbent.

Doping causes a bathochromic shift, or red shift, which increases the wavelength and reduces the bandgap of $ZnWO_4$ nanomaterial, thereby enhancing its photocatalytic properties. The 1Na1Mg1Ti doped $ZnWO_4$ was particularly effective in degrading MG, similar to other nanomaterials studied. This doped material, in the monoclinic phase, had the smallest crystallite size of 4.22 nm and a BET surface area of 156.92 m^2/g. In comparison, undoped $ZnWO_4$ had a crystallite size of 14.51 nm and a BET surface area of 24.73 m^2/g. Consequently, 1Na1Mg1Ti doped $ZnWO_4$ disperses better in dyeing wastewater and has more active sites for trapping impurities [25]. Table 4 summarizes the photocatalytic degradation of MG, achieving efficiencies of 48.62 %, 99.93 %, 99.86 %, 94.81 %, and 97.12 % using $ZnWO_4$, 1Na1Mg1Ti-$ZnWO_4$, 1Na/1Mg/2Ti-$ZnWO_4$, 1Na/2Mg/1Ti-$ZnWO_4$, and 2Na/1Mg/1Ti-$ZnWO_4$, respectively, compared to results from previous studies. It is obvious that the performance of the developed $ZnWO_4$-based photocatalyst is comparable to that of other materials. This may be linked to the triple doping effect of metals on $ZnWO_4$.

3.10.3. *Mechanism for the multiple doped $ZnWO_4$ nanocomposites*

The energy band structure comprises distinct valence and conduction bands separated by a forbidden band. When light with higher energy than the band gap is absorbed, valence electrons move to the conduction band, leaving behind holes. In the case of $ZnWO_4$, poor crystallinity increases lattice defects, acting as additional holes. This boosts nanoparticle activity as free electrons and holes migrate to the catalyst's inner pores, reacting with oxygen and water to generate hydroxyl radicals (*OH) and superoxide anions (O_2^-). These reactive species degrade organic compounds in dye wastewater into CO_2 and H_2O (Fig. S9). Metal doping involves replacing Zn^{2+} and W^{6+} lattice positions with Na+, Mg^{2+}, and Ti^+ ions (Fig. S10). Photogenerated electrons in Na/Mg/Ti rapidly oxidize to form superoxide anion radicals (O_2^{*-}),

Table 4
Photodegradation of MG dyeing wastewater compared to previous literature.

Photocatalysts	Method of synthesis	Nature of the dopant and doping	BET surface area (m^2/g)	Band gap energy (eV) or crystallite size	MG removal	Number of reusability cycle	References
N/Na/Fe-TiO_2	Hydrothermal	Multiple	800.16	2.10 nm	96.57 %	5	Amigun et al. [45]
Ni/Kaolin	Wet impregnation	Mono	31.2	–	98.87 %	–	Moumen et al. [46]
$ZnVFeO_4$	Precipitation	Tricomposite	7.38	1.90 eV	98.0 %	5	Mostafa and Amdeha [47]
$ZnWO_4$@BCN/N	Solgel	Multiple	45.43	–	75.78 mg/g	8	Abubakar et al. [25]
$BaTiO_3$	Pechini sol–gel	Mono	–	3.03 eV/ 22.27 nm	93.94 %	4	Al-wasidi and Abdelrahman [48]
Organo-bentonite/ C_3O_4	Direct Intercalation	Hybrid	–	–	100 %	5	Abdel Salam et al. [49]
CeO_2	Co-precipitation	–	189.3	3.7 nm	98.0 %	5	Borgohain and Rashid [50]
FeO_4@AJPL	Co-precipitation	Mono	38.44	–	318.3 mg/g	2	Alorabi [51]
Ag/ZnCO-ZIF	Simple Solvothermal	Mono	–	–	99.1 %	4	Dang et al. [52]
$CuFe_2O_4$	One pot energy saving solution combustion synthesis	–	128	17 nm	85 %	4	Vergis et al. [53]
$CuFe_2O_4$-Fe_2O_3	Modified Pechini	HybridHybrid	–	1.92 eV	100 %	45	Silva et al. [54]
$ZnWO_4$-Carbon	MethodSolvothermal method			3.87 eV	71.4 %		He et al. [10]
$ZnWO_4$	Sol-gel	–	24.74		48.62 %	5	This study
1Na/1Mg/1Ti-$ZnWO_4$ 1Na/1Mg/2Ti-$ZnWO_4$ 1Na/2Mg/1Ti-$ZnWO_4$ 2Na/1Mg/1Ti-$ZnWO_4$	Co-precipitationCo-precipitationCo-precipitationCo-precipitation	Multiple	156.93156.26146.70146.30		99.93 % 99.86 % 94.81 % 97.12 %	5	This studyThis studyThis studyThis study

while holes react with water molecules, yielding *OH. *OH primarily forms through oxidation pathways, subsequently reacting with dye molecules, producing CO_2 and H_2O intermediates. Introducing Na^+, Mg^{2+}, and Ti^+ onto the Zn and W lattice layers significantly reduces the bandgap. During catalysis, these dopants capture electrons, suppressing the recombination of electron-hole pairs, thereby enhancing the photocatalytic activity of metal and non-metal-doped $ZnWO_4$. The suggested method for the breakdown of organic compounds by the nanocomposites when exposed to sunlight is described; a similar process also takes place in the undop$_{ed\ ZnWO4}$ nanomaterials.

$$\text{Na-Mg-Ti} + hv \rightarrow eCB^- + hVB^+ \quad (9)$$

$$H_2O \rightarrow OH^- + H^+ \quad (10)$$

$$hVB^+ + H_2O \rightarrow OH^\circ + H^+ \quad (11)$$

$$hVB^+ + OH^- \rightarrow OH^\circ \quad (12)$$

$$eCB^- + O_2 \rightarrow O_2^{*-} \quad (13)$$

$$O_2^{*-} + 2H^+ + eCB^- \rightarrow H_2O_2 \quad (14)$$

$$O_2^{*-} + H^+ \rightarrow HO_2^{*-} \quad (15)$$

$$HO_2^{*-} + HO_2^{*-} \rightarrow H_2O_2 + \frac{1}{2}O_2 \quad (16)$$

$$H_2O_2 + H^+ + eCB^- \rightarrow OH^\circ + H_2O \quad (17)$$

$$OH^\circ + \text{organic dyes} \rightarrow \text{intermediates} + H_2O + CO_2 \quad (18)$$

$$O_2^{*-} + \text{organic dyes} \rightarrow \text{intermediates} + H_2O + CO_2 \quad (19)$$

3.10.4. Toxicity test using juvenile fish larvae

The survival rate of juvenile fish was tested in five water samples: untreated water ("RAW"), water treated with $ZnWO_4$ nanoparticles, water treated with a 1Na1Mg1Ti doped $ZnWO_4$ nanocomposite ("1Na1Mg1Ti") and tap water as a control ("tap water"), as shown in Fig. S11. Initially, the fish exhibited no significant reactions upon exposure. However, within 24 h, over 50 % of the fish in the RAW sample died, and by the third day, none survived. In the $ZnWO_4$ sample, five fish died, representing 75 %. In the first 24 h, one more died subsequently, and the rest survived. In the 1Na1Mg1Ti sample, all fish survived the first 48 h, with only one fish died by the third day. All 20 fishes (100 %) in the tap water sample survived the experiment. The most suitable water for supporting aquatic life was the 1Na1Mg1Ti treated sample. The toxicity order from highest to lowest as a function of survival rate was RAW (35 %) > $ZnWO_4$ (75 %) > 1Na1Mg1Ti (99 %) > Tap water (100 %). Studies indicate that wastewater from indigenous dyeing processes containing MG is highly toxic to aquatic life, causing severe physiological issues [55]. Rodriguez-Loaiza et al. [56] found that industrial wastewater treated biologically improved the survival rate of *Vibrio fischeri* from less than 60 % to 82 %. Thus, using $ZnWO_4$ triple-doped with sodium, magnesium, and titanium was more effective for detoxifying wastewater than biological processes alone, which do not sufficiently detoxify water to support aquatic and plant life.

3.10.5. Regeneration study

Fig. S12 illustrates the percentage of nanomaterial removal after each cycle. The study found that 1Na1Mg1Ti-doped $ZnWO_4$ nanocomposite materials consistently showed the highest efficiency in removing MG dye, even after five cycles of use. The efficiency of all nanomaterials remained high at the fifth cycle, with minimal decline. While the pure $ZnWO_4$ had relatively low removal efficiency, it still maintained consistent performance across cycles. The 1Na1Mg1Ti-

doped $ZnWO_4$ achieved a removal rate of 75.3 %, compared to 40.1 % for the undoped $ZnWO_4$. This enhanced performance is attributed to the larger surface areas of the doped nanocomposites.

3.11. Characterization of spent nanocrystals

3.11.1. FTIR analysis of undoped $ZnWO_4$ and multiple metals after photocatalysis

The FTIR spectra of the synthesized $ZnWO_4$ nanocomposite samples were examined both before and after photocatalysis. The corresponding spectrum is depicted in Fig. S13. An absorption band at around 665 cm^{-1} was attributed to W-O bending vibrations [13], while another band at 884 cm^{-1} indicates Zn-O-W stretching and bending vibrations [57]. Bands in the ranges of 1541 cm^{-1} to 1401 cm^{-1} and 3449 cm^{-1} to 3156.5 cm^{-1} are indicative of H-O-H bending vibrations [13]. Significant changes in vibrations from 500-1000 cm^{-1} for the doped $ZnWO_4$ nanocomposites after catalysis were observed, and these could be attributed to structural and chemical modifications induced by the catalytic reaction. The region that corresponds to W-O stretching and bending modes is sensitive to doping, lattice distortion, and surface interactions. The interactions with reactants or intermediates can alter bond strengths, causing shifts or intensity changes in these modes, as well as degradation and recombination of dopants, which may further contribute to these vibrational changes. Research has demonstrated that doping enhances the intensity of adsorption bands in 1Na1Mg1Ti-doped $ZnWO_4$ compared to undoped $ZnWO_4$. The removal of MG from the aqueous matrix did not impact the functional groups in the nanocomposites used. However, the intensity of the peaks in undoped $ZnWO_4$ was lower than in the doped $ZnWO_4$ nanocomposites, indicating that doped samples are more stable. The peaks in doped $ZnWO_4$ remain sharper and more intense, showing the material's stability and suitability for repeated use, which can result in cost savings [25].

3.11.2. XRD analysis of multiple doped $ZnWO_4$ nanocomposites after photocatalysis

The phase structures of $ZnWO_4$ nanocomposites doped with the selected metals were examined through XRD analysis following photocatalysis, with corresponding spectra illustrated in Fig. S14. The XRD results revealed prominent diffraction peaks at 2θ values of 18.90°, 24.57°, 30.47°, 36.31°, 41.14°, 54.26°, 61.65°, and 64.20°, corresponding to miller indices (100), (110), (111), (021), (121), (202), (113), and (311). Notably, there was a noticeable broadening and weakening of peaks in the doped $ZnWO_4$ nanomaterials, attributed to oxygen displacement and impurity introduction on the material's surface. Despite this, the phase remained unchanged post-photocatalysis, as evidenced by similar XRD profiles before and after the process, albeit with slight alterations in relative peak intensities. The observed peak broadening may indicate a partial loss of crystallinity due to the introduction of pollutant ions. All nanocomposites retained a monoclinic phase of $ZnWO_4$ with JCPDS no. 15–0554 and a space group of p2/c. Consistently, Aibade and Oluwana (2021) reported minimal variations in peak patterns pre- and post-photocatalysis, affirming the retention of the hexagonal covellite phase in CuS nanoparticles [58,17].

4. Conclusion

$ZnWO_4$ nanocomposite, which was triple-doped with Na, Mg, and Ti metals, exhibited significant effectiveness in treating indigenous dyeing effluent. The ratio of the dopant mixture affected the spherical shape, uniform distribution, and growth orientation of the doped nanocomposite. Likewise, the surface area exhibited an increasing trend with the addition of multiple metal dopants, arranged as follows: $ZnWO_4$ < 2Na1Mg1Ti < 1Na2Mg1Ti < 1Na1Mg2Ti < 1Na1Mg1Ti. All the nanomaterials that were doped exhibited a type IV isotherm, indicating the presence of mesoporosity that is characterized by cylindrical pores with open ends. Box-Behnken design optimization identified the optimal conditions for MG removal (99.93 % efficiency) using 1Na1Mg1Ti-doped $ZnWO_4$ (catalyst load: 0.7 g, contact time: 35 min, pH: 12). Multiple metal doping enhanced MG removal by 34.37 %. 1Na1Mg1Ti-doped $ZnWO_4$ outperformed $ZnWO_4$ nanoparticles, retaining effectiveness after repeated applications. Treated wastewater supported aquatic life compared to untreated, with 1Na1Mg1Ti-doped $ZnWO_4$ showing superior performance. The nanocomposite's photocatalytic behavior for MG removal was attributed to its lower band gap energy and higher surface area compared to $ZnWO_4$ nanoparticles.

CRediT authorship contribution statement

Hassana Ladio Abubakar: Writing – original draft, Visualization, Methodology, Formal analysis, Data curation, Conceptualization. **Jimoh Oladejo Tijani:** Writing – review & editing, Visualization, Formal analysis, Data curation. **Saheed Mustapha:** Writing – review & editing, Visualization, Formal analysis, Data curation. **Ambali Saka Abdulkareem:** Writing – review & editing, Visualization, Formal analysis, Data curation. **Mann Abdullahi:** Writing – review & editing, Visualization, Formal analysis, Data curation. **Titus Chinedu Egbosiuba:** Writing – review & editing, Supervision, Formal analysis, Data curation. **Francis Ntumba Muya:** Writing – review & editing, Visualization, Formal analysis, Data curation. **Omar H. Abd-Elkader:** Writing – review & editing, Visualization, Formal analysis, Data curation. **Hamad A. Al-Lohedan:** Writing – review & editing, Visualization, Formal analysis, Data curation. **Alechine Emmanuel Ameh:** Writing – review & editing, Formal analysis, Data curation. **Abdelrahman O. Ezzat:** Writing – review & editing, Visualization, Formal analysis, Data curation.

Declaration of competing interest

The authors declare that they have no known competing financial interests or personal relationships that could have appeared to influence the work reported in this paper.

Acknowledgment

The authors acknowledged Tertiary Education Trust Fund, Nigeria (TETF/ES/DR & DCE/NRF/2021/SETI/WAS/0063/VOL.1) and Africa Centre of Excellence for Mycotoxin and Food Safety, Federal University of Technology, Minna, Nigeria for the sponsorship. The authors acknowledge the financial support through the Researchers Supporting Project number (RSP2025R54), King Saud University, Riyadh, Saudi Arabia.

Ethical approval

Not applicable.

Consent to participate

Not applicable.

Consent to publication

Not applicable.

Appendix A. Supplementary data

Supplementary data to this article can be found online at https://doi.org/10.1016/j.inoche.2025.114012.

Data availability

All relevant data are within the paper. No new data were created or analyzed in this study.

References

[1] J.S. Jeyaprakash, M. Rajamani, C.L. Bianchi, M. Ashokkumar, B. Neppolian, Highly efficient ultrasound driven Cu-MOF/$ZnWO_4$ heterostructure: An efficient visible-light photocatalyst with robust stability for complete degradation of tetracycline, Ultrason. Sonochem. 100 (2023) 106624.

[2] M.R. Tamtam, R. Koutavarapu, J. Shim, InVO4 nanosheets decorated with $ZnWO_4$ nanorods: A novel composite and its enhanced photocatalytic performance under solar light, Environ. Res. 227 (2023) 115735.

[3] R. Naveen, M.C. Rao, K. Syed, J. Shim, R. Koutavarapu, Exploring the mechanistic insights of Fe3+-doped LiZnBO3 nanosheets for visible light-driven photocatalytic degradation of mineral pollutants in wastewater, J. Environ. Chem. Eng. 11 (5) (2023) 110565.

[4] R. Naveen, M.C. Rao, M.R. Tamtam, R. Koutavarapu, Enhancing photocatalytic degradation of potassium butyl xanthate in mineral processing wastewater: Novel VO^{2+}-doped $LiZnBO_3$ nanosheets under visible light, Surf. Interfaces 42 (2023) 103459.

[5] F. Zhang, X. Wang, H. Liu, C. Liu, Y. Wan, Y. Long, Z. Cai, Recent Advances and Applications of Semiconductor Photocatalytic Technology, Appl. Sci. 9(12), 2489 (2019) 1–43.

[6] J. Liu, Y. Li, X. Zhang, V.K. Sharma, C.M. Sayes, Effects of ascorbate and carbonate on the conversion and developmental toxicity of halogenated disinfection by products during boiling of tap water, Chemosphere 254 (2020) 126890, https://doi.org/10.1016/j.chemosphere.2020.126890.

[7] Liu X, Shu J, Wang H, Jiang z, Xu L, & Liu C (2023). One-pot preparation of a novel $CoWO_4$/$ZnWO_4$ p-n heterojunction photocatalyst for enhanced photocatalytic activity under visible light irradiation. Journal of Physics and Chemistry of Solids,172, 111061.

[8] D.R. Vaddi, K. Vinukonda, R.K. Patnala, Y. Kanithi, T.R. Gurugubelli, J. Bae, R. Koutavarapu, D.Y. Lee, J. Shim, Effect of yttrium doping on the crystal structure, optical, and photocatalytic properties of hydrothermally synthesized ZnO nanorods, Mater. Sci. Eng. B 296 (2023) 116664.

[9] V. Faka, S. Tsoumachidou, M. Moschogiannaki, G. Kiriakidis, I. Poulios, V. Binas, $ZnWO_4$ nanoparticles as efficient photocatalyst for degradation of para-aminobenzoic acid: Impact of annealing temperature on photocatalytic performance, J. Photochem. Photobiol. A Chem. 113002 (2020), https://doi.org/10.1016/j.jphotochem.2020.113002.

[10] H. He, Z. Luo, C. Yu, Multifunctional $ZnWO_4$ nanoparticles for photocatalytic removal of pollutants and disinfection of bacteria, J. Photochem. Photobiol. A Chem. 401 (2020) 112735.

[11] G. Chena, F. Wanga, J. Yu, H. Zhang, X. Zhang, Improved red emission by codoping Li^{3+} in $ZnWO_4$:Eu^{3+} phosphors, J. Mol. Struct. 1128 (2017) 1–4.

[12] M. Rahmani, T. Sedaghat, Nitrogen-doped $ZnWO_4$ nanophotocatalyst: synthesis, characterization and photodegradation of methylene blue under visible light, Res. Chem. Intermed. 45 (2019) 5111–5124.

[13] A.K. Paliki, S.M. Botsa, B.B.V. Sailaja, Catalytic activity of graphene oxide hybridized $ZnWO_4$ for dyes degradation and oxidation of functionalized benzyl alcohols, MOJ Biorganic and Organic Chemistry 2 (5) (2018) 230–234.

[14] J. Nie, Q.U. Hassan, Y. Jia, J. Gao, P. Peng, J. Lu, F. Zhang, G. Zhu, Q. Wang, La-Doped ZnWO4 nanorods with enhanced photocatalytic activity for NO removal: effects of La doping and oxygen vacancies, Inorg. Chem. Front. (2019), https://doi.org/10.1039/c9qi01152h.

[15] R. Naveen, M.C. Rao, R. Koutavarapu, M.R. Tamtam, Mechanistic insights into chromium ions-doped lithium zinc borate nanosheet photocatalysis for mineral pollutant removal, Mater. Sci. Semicond. Process. 175 (2024) 108259.

[16] Y. Pan, W. Zhang, Z. Hu, Z. Feng, L. Ma, D. Xiong, P. Hu, Y. Wang, H. Wu, L. Luo, Synthesis of Ti^{4+}-doped $ZnWO_4$ phosphors for enhancing photocatalytic activity, Journal of Luminescence, 206, ISSN 267–272 (2019) 0022–2313.

[17] D.P. Dutta, P. Raval, Effect of transition metal ion (Cr^{3+}, Mn^{2+} and Cu^{2+}) doping on the photocatalytic properties of $ZnWO_4$ nanoparticles, J. Photochem. Photobiol. A Chem. 357 (2018) 193–200.

[18] R. Naveen, M.C. Rao, J. Shim, M.R. Tamtam, R. Koutavarapu, Morphological and bandgap engineering of $LiZnBO_3$ nanostructures via hydrothermal process for enhanced solar light photocatalysis, J. Mater. Sci. Mater. Electron. 35 (15) (2024) 1036.

[19] G. Xiong, W. Zhang, Z.-F. Hu, Z.-Y. Feng, P. Hu, L. Ma, L. Luo, Photocatalytic activity of $ZnWO_4$ phosphors doped with Li impurities, J. Lumin. (2018), https://doi.org/10.1016/j.jlumin.2018.10.053.

[20] H.L. Abubakar, J.O. Tijani, A.S. Abdulkareem, T.C. Egbosiuba, M. Abdullahi, S. Mustapha, E.A. Ajiboye, Effective removal of malachite green from local dyeing wastewater using zinc-tungstate based materials, Heliyon 9 (9) (2023).

[21] V.S. Vinila, J. Isac, Synthesis and structural studies of superconducting perovskite $GdBa_2Ca_3Cu_4O_{10}$. 5+ δ nanosystems, in: Design, fabrication, and characterization of multifunctional nanomaterials, Elsevier, 2022, pp. 319–341.

[22] C.A. Uko, J.O. Tijani, A.S. Abdulkareem, S. Mustapha, T.C. Egbosiuba, E. Muzenda, Adsorptive properties of MgO/WO_3 nanoadsorbent for selected heavy metals removal from indigenous dying wastewater, Process Saf. Environ. Prot. 162 (2022) 775–794.

[23] J.O. Tijani, U.O. Momoh, R.B. Salau, M.T. Bankole, A.S. Abdulkareem, W.D. Roos, Synthesis and characterization of $Ag_2O/B_2O_3/TiO_2$ ternary nanocomposites for photocatalytic mineralization of local dyeing wastewater under artificial and natural sunlight irradiation, Environ. Sci. Pollut. Res. 26 (2019) 19942–19967.

[24] Raizada P., Shandilya P., Singh P. & Thakur P. (2017 b). Solar light-facilitated oxytetracycline removal from the aqueous phase utilizing a H_2O_2/$ZnWO_4$/CaO catalytic system. Journal of Taibah University for Science, 11(5), 689–699.

[25] H.L. Abubakar, J.O. Tijani, S.A. Abdulkareem, A. Mann, S. Mustapha, A review of the applications of zinc tungstate ($ZnWO_4$) photocatalyst for wastewater treatment, Heliyon 8 (2022) e09964.

[26] A.G. Habte, F.G. Hone, F.B. Dejene, Influence of Cu-doping concentration on the structural and optical properties of SO_2 nanoparticles by coprecipitation route, Journal of Nanomaterials (2022) 5957125.

[27] Sharma R. K., Yadav S., Dutta S., Kale H. B., Warkad W. I., Zbořil R., Varma R. S., Gawande M. B. (2021). Silver nanomaterials: synthesis and (electro/photo) catalytic applications. Chemical Society Reviews 2021, 50(20), 11293-11380.

[28] C. Rao, W. Zhang, Z. Hu, Z. Feng, Y. Chen, Y. Pan, P. Hu, Y. Wang, W. Zhao, Enhancing the photocatalytic activity of La/Y Co-doped $ZnWO_4$ under UV irradiation, Key Eng. Mater. 842 (2019) 214–222.

[29] J.O. Tijani, E.I. Odeh, S. Mustapha, T.C. Egbosiuba, A.I. Daniel, A.S. Abdulkareem, F.N. Munya, Photocatalytic, electrochemical, antibacterial and antioxidant behavior of carbon-sulfur co-doped zirconium (IV) oxide nanocomposite, Cleaner Chem. Eng. 3 (2022) 100034.

[30] R. Yousefi, J. Beheshtian, S.M. Sayed-Talebi, H.R. Azimi, F. Jamali-Sheini, Experimental and theoretical study of enhanced photocatalytic activity of Mg-Doped ZnO NPs and ZnO/rGO Nanocomposites, Chemistry-an Asian Journal 13 (2) (2018) 194–203.

[31] Osotsi M. I., Macharia D. K., Zhu B., Wang Z., Shen X., Liu Z., Zhang L. & Chen Z. (2018). Synthesis of $ZnWO_4$-x nanorods with oxygen vacancy for efficient photocatalytic degradation of tetracycline, Progress in Natural Science: Materials International, 28:4, 408-415, ISSN 1002-0071.

[32] J.O. Tijani, M.N. Abdullahi, M.T. Bankole, S. Mustapha, T.C. Egbosiuba, M. Ndamitso, A.S. Abdulkareem, E. Muzenda, Photocatalytic and toxicity evaluation of local dyeing wastewater by aluminium/boron doped WO_3 nanoparticles, J. Water Process Eng. 44 (2021) 102376.

[33] G.V. Geetha, R. Sivakumar, C. Sanjeeviraja, V. Ganesh, Photocatalytic degradation of methylene blue dye using $ZnWO_4$ catalyst prepared by a simple co-precipitation technique, J. Sol-Gel Sci. Technol. 97 (3) (2021) 572–580.

[34] G.V. Geetha, R. Sivakumar, Y. Slimani, C. Sanjeeviraja, E. Kannapiran, Rare earth (RE: La and Ce) elements doped $ZnWO_4$ nanoparticles for enhanced photocatalytic removal of methylene blue dye from aquatic environment, Phys. B Condens. Matter 639 (2022) 414028.

[35] L. Tian, Y. Rui, K. Sun, W. Cui, W. An, Surface decoration of $ZnWO_4$ nanorods with Cu_2O nanoparticles to build heterostructure with enhanced photocatalysis, Nanomaterials 8 (1) (2018) 33.

[36] B.E. Azimi, A. Badiei, J.B. Ghasemi, Efficient removal of malachite green from wastewater by using boron-doped mesoporous carbon nitride, Appl. Surf. Sci. 469 (2019) 236–245.

[37] M. Arshad, S. Ehtisham-ul-Haque, M. Bilal, N. Ahmad, A. Ahmad, M. Abbas, J. Nisar, M.I. Khan, A. Nazir, A. Ghaffar, M. Iqbal, Synthesis and characterization of Zn doped WO_3 nanoparticles: photocatalytic, antifungal and antibacterial activities evaluation, Mater. Res. Express 7 (2020) 015407.

[38] F.Z. Janani, H. Khiar, N. Taoufik, A. Elhalil, M. Sadiq, S. Mansouri, N. Barka, ZnO-Zn_2TiO_4 heterostructure for highly efficient photocatalytic degradation of pharmaceuticals, Environ. Sci. Pollut. Res. (2022), https://doi.org/10.1007/s11356-022-22791-6.

[39] Muhammad Y. K., Manzoor A., Sana S., Saleem I., Faisal N. & Javed (2019). Visible light active indigo dye/graphene/WO_3 nanocomposites with excellent photocatalytic activity. Journal of Materials, Research and Technology, 8(3): 3261–3269.

[40] C. Hanane, E.A. Alaa, D. Mustapha, F. Sophie, A statistical modeling-optimization approach for efficiency photocatalytic degradation of textile azo dye using cerium-doped mesoporous ZnO: A central composite design in response surface methodology, Chem. Eng. Res. Des. 171 (2021) 198–212.

[41] N. Jamal, A. Radhakrishnan, R. Raghavan, B. Beena, Efficient photocatalytic degradation of organic dye from aqueous solutions over zinc oxide incorporated nanocellulose under visible light irradiation, Main Group Met. Chem. 43 (1) (2020) 84–91.

[42] A.H. Ghasemi, M.J. Zoqi, P. Zanganeh Ranjbar, Enhanced photocatalytic degradation of methylene blue using a novel counter-rotating disc reactor, Front. Chem. 12 (2024).

[43] R. Farouq, Coupling adsorption-photocatalytic degradation of methylene blue and maxilon red, J. Fluoresc. 32 (4) (2022) 1381–1388.

[44] R. Raliya, C. Avery, S. Chakrabarti, Photocatalytic degradation of methyl orange dye by pristine titanium dioxide, zinc oxide, and graphene oxide nanostructures and their composites under visible light irradiation, Appl. Nanosci. 7 (5) (2017) 253–259.

[45] A.T. Amigun, F.A. Adekola, O. Tiani, S. Mustapha, Photocatalytic degradation of Malachite green dye using nitrogen/sodium/iron-TiO_2 nanocatalysts, Results Chem. 4 (2022) 100480.

[46] A. Moumen, Y. Belhocine, N. Sbei, S. Rahali, F.A. Ali, F. Mechati, F. Hamdaoui, M. Seydou, Removal of malachite green dye from aqueous solution by catalytic wet oxidation technique using Ni/Kaolin as catalyst, Molecules 27 (21) (2022) 7528.

[47] E.M. Mostafa, E. Amdeha, Enanced photocatalytic degradation of malachite green dye by highly stable visible light-responsive Fe-based tri-composite photocatalyst, Enhanced Science and Pollution Research 29 (2022) 69861–69874.

[48] Al-Wasidi A. S. & Abdelrahman E. A. (2023). Significant photocatalytic decomposition of malachite green dye in aqueous solutions utilizing facilely synthesized barium titanate nanoparticles. Discover Nano, 28; 18(1):97.

[49] S.M. Abdel, M.R. Abukhadra, A. Adlii, Insight into the adsorption and photocatalytic behaviors of an organo-bentonite/CO_3O_4 green nanocomposite for malachite green synthetic dye and Cr(VI) metal ions: Application and Mechanisms, ACS Omega 5 (6) (2020) 2766–2778.

[50] X. Borgohain, E. Das, M.H. Rashid, Facile synthesis of CeO_4 nanoparticles for enhanced for enhanced removal of malachite green dye from an aqueous environment, Mater. Adv. 4 (2) (2023) 683–693.
[51] A. Alorabi, Effective removal of Malachite green from aqueous solutions using magnetic nanocomposite: Synthesis, Characterization and equilibrium study, Adsorpt. Sci. Technol. 6 (2021) 1–15.
[52] G.H. Dang, T.A. Le, K.A. Ta, T.N. Ho, T.V. Pham, V.H. Doan, H.V. Luong, Removal of congo red and malachite green from aqueous solution using heterogeneous Ag/ZnCo-ZIF catalyst in the presence of hydrogen peroxide, Green Processes Synth. 9 (1) (2020) 567–577.
[53] B.R. Vergis, R.H. Krishna, N. Kottam, B.M. Nagabushana, R. Sharath, B. Darukaprasad, Removal of Malachite green from aqueous solution by magnetic $CuFe_2O_4$ nano-adsorbent synthesized by one pot solution combustion method, Journal of Nanostructure in Chemistry 8 (2018) 1–12.
[54] E. Silva, I.L. Brasileiro, V.S. Madeira, B. Aranha de Farias, M.L. Ramalho, E. Rodriguez-Aguado, E. Rodriguez-Castellon, Reusable $CuFe_2O_4$-Fe_2O_3 catalyst synthesis and application for the heterogenous photo-Fenton degradation of methylene blue in visible light, J. Environ. Chem. Eng. 8 (5) (2020) 104132.
[55] B.C. Almroth, J. Cartine, C. Jonander, M. Karlsson, J. Langlois, M. Lindstrom, J. Lundin, N. Melander, A. Pesqueda, I. Rahmqvist, J. Renaux, J. Roos, F. Spilsbury, J. Svalin, H. Vestlund, L. Zhao, N. Asker, G. Asmonaite, L. Birgersson, T. Boloori, F. Book, T. Lammel, J. Sturve, Assessing the effects of textile leachates in fish using multiple testing methods: from gene expression to behavior, Ecotoxicology and Environmental Safety, 207, ISSN 111523 (2021) 0147–6513.
[56] D.C. Rodríguez-Loaiza, O. Ramírez-Henao, G.A. Peñuela-Mesa, Assessment of toxicity in industrial wastewater treated by biological processes using luminescent bacteria, Actualidades Biológicas 38 (105) (2016) 211–216.
[57] J. Yesuraj, S.A. Suthanthiraraj, Bio-molecule templated hydrothermal synthesis of $ZnWO_4$ nanomaterial for high-performance supercapacitor electrode application, J. Mol. Struct. 1181 (2019) 131–141.
[58] C.I.M. Rodriguez, M.A.L. Alvarez, J.F. Rivera, G.G.C. Arizaga, C.R. Michel, α-Ga_2O_3 as a photocaalyst in the degradation of Malachite Green, ECS J. Solid State Sci. Technol. 8 (7) (2019) 3180–3186.